RSC Sustainability

ROYAL SOCIETY OF CHEMISTRY

PAPER

View Article Online
View Journal

Check for updates

Cite this: DOI: 10.1039/d6su00083e

Recycling of solar cells recovered from waste panels into efficient silicon-based composite electrodes for energy-storage applications

Soumya Ranjan Nayak,[ab] Manisha Balkhandia,[ab] Imran Chhimpa[ab]
and Sushil Kumar *[ab]

Received 10th February 2026
Accepted 26th April 2026

DOI: 10.1039/d6su00083e

rsc.li/rscsus

The significant increase in the cumulative installation capacity of solar photovoltaic modules as a source of renewable energy has led to a tremendous increase in the volume of end-of-life (EoL) solar modules, creating an essential requirement for sustainable waste management. In this work, an eco-friendly and less toxic recycling process has been developed to recover silicon and native silica (SiO_2) from discarded crystalline silicon solar cells for their use as functional electrode materials for different faradaic energy storage applications. The recovered materials were chemically treated and employed to fabricate slurry-coated electrodes over copper foil. This recovered silicon was also deposited over various substrates, including indium tin oxide (ITO)-coated glass and graphite sheets, to examine how the substrates affect the overall charge-storage reaction mechanism. The recycled material was structurally characterized using XPS, XRD, XRF and Raman spectroscopy, whereas morphological properties were analysed by employing TEM, SEM, EDAX and AFM. Thermal analysis was carried out using TGA to evaluate the thermal stability and compositional changes of the recycled silicon powder. The surface properties were also analysed using BET to determine the surface area and porosity of the powder. Electrochemical characterizations, including CV, EIS and GCD, were also performed on the prepared electrodes. This study presents an eco-friendly solution by integrating recycled photovoltaic waste into electrode materials for use in Li-ion electrochemical systems, with an emphasis on substrate-dependent faradaic charge storage behaviour. It further highlights substrate-dependent charge storage with electrodes formed on ITO and graphite sheets showing different charge-storage characteristics. The prepared electrodes over Cu foils, ITO and graphite sheets exhibited specific capacitance values of 143.23 Fg^{-1}, 30.53 Fg^{-1} and 163.92 Fg^{-1}, respectively.

Sustainability spotlight

The significant increases in the cumulative installation capacity of solar photovoltaic modules as a source of renewable energy have led to a tremendous increase in the volume of end-of-life (EoL) solar modules, creating an essential requirement for sustainable waste management. Our research delivers crucial insights into the substrate-dependent charge storage and electrochemical characteristics of recycled silicon derived from end-of-life photovoltaic modules using a less toxic approach, highlighting the circular economy strategies through the integration of photovoltaic recycling. We have investigated Raman effects, revealing vibrational modes of crystalline silicon, along with the Si–O stretching mode that indicates the partial surface oxidation of silicon. Furthermore, the electrodes were prepared from recycled silicon powder over different substrates, and their electrochemical characterizations further validate our findings.

1 Introduction

In recent decades, the installation capacity of solar photovoltaic (PV)[1,2] module has been continuously increasing, resulting in the substantial accumulation of large quantities of solar waste that require urgent end-of-life (EoL)[3–5] solutions. This solar waste flux presents the PV industry with an unprecedented waste management challenge.[6,7] As per an International Renewable Energy Agency (IRENA) report, world renewable energy capacity amounted to 4448 GW at the end of 2024.[8] Solar accounted for the largest share (nearly 42%) of the global total, with a capacity of 1865 GW.[9] India's solar power capacity was ~133 GW by the end of 2025.[10] However, photovoltaic panels installed around the late 1990s and early 2000s have already reached their end of life due to a limited lifespan of 25 to 30 years, generating large volumes of solar PV waste. This growing challenge highlights the urgent need for effective recycling strategies and policy frameworks to manage end-of-life solar panels, thereby ensuring

---

[a] *CSIR- National Physical Laboratory, Dr K. S. Krishnan Marg, New Delhi 110012, India. E-mail: skumar@nplindia.org*

[b] *Academy of Scientific and Innovative Research (AcSIR), Ghaziabad – 201002, India*

a sustainable energy cycle.[11,12] The end-of-life pressure, combined with manufacturing residues such as kerf and cutting waste generated during wafering and module fabrication, presents both an environmental challenge and a valuable resource recovery opportunity.[13,14] Silicon recovered from PV wafers represents a high-value material for reuse because of its intrinsic electrochemical properties, which far exceed those of conventional graphite anodes used in lithium-ion batteries (LIBs).[15,16] Silicon possesses a theoretical specific capacity of around 4200 mAh g^{-1}, which is more than ten times higher than that of graphite (372 mAh g^{-1}), making it an exceptionally attractive high-capacity anode precursor.[17,18] Recent studies have demonstrated that nano-structured or processed PV silicon can be converted into active anode materials for lithium-ion batteries, providing direct value addition from end-of-life modules.[7,19] Moreover, the SiO_x/SiO_2 content naturally present in recycled PV silicon can be tuned to form Si–SiO_x hybrid phases that contribute an inert buffering matrix during lithiation, an effect exploited in several recent anode designs to enhance electrochemical stability.[20,21] Also, as one of the most abundant elements (second highest) in the Earth's crust, silicon offers high availability and environmental sustainability as an anode material for Li-ion batteries.[22,23] When Si is used as an active material in lithium-ion batteries, it undergoes significant volume changes during repeated lithiation and de-lithiation due to its intrinsic properties.[24] Several advances have been achieved in silicon anode development through improved synthesis strategies, including template-based routes, chemical vapor deposition (CVD), sol–gel, hydrothermal, spray-drying, and self-assembly methods. These approaches enable precise control over nanosheet size and structure, while surface engineering and composite design further enhance electrochemical performance and battery compatibility. Compositing carbon materials with Si helps accommodate the tension within the electrodes and enhance their conductivity.[25] Zhang *et al.*[26] fabricated carbon nanotube (CNT)-interconnected SiO_x/C@C spherical structures with an outer carbon layer, achieving a high reversible capacity of 857.7 mAh g^{-1} at 0.1 A g^{-1}, good cycling stability of 333.3 mAh g^{-1} at 0.1 A g^{-1}, and an excellent rate capability of 333.3 mAh g^{-1} at 10 A g^{-1}. Similarly, Fan *et al.*[27] reported the encapsulation of carbon-coated Si nanoparticles within a CNT-reinforced carbon framework derived from ZIF-67, delivering a stable capacity of 680 mAh g^{-1} after 1000 cycles at a current density of 1 A g^{-1}. While combining silicon nanoparticles with carbon nanotubes improves electrode performance, significant issues still exist. Insufficient bonding at the Si–C interface can cause structural failure during repeated cycling.[28] Therefore, there is a strong need for simple, economical fabrication strategies that can deliver Si/C electrodes with high conductivity and durable cycle stability. The present work explores the electrochemical performance of Si-CNT electrodes developed using silicon derived from waste PV modules, giving a second life to the embedded silicon post EoL. The novelty of the work lies in the development of a purification and composite fabrication process that yields Si-CNT electrodes with reasonable cycling stability, and a systematic investigation of the quality of the recycled PV silicon and its impact on CNT-mediated electrochemical performance. The research demonstrated that recycled silicon from solar panel waste can achieve stable performance for about 500 cycles. Therefore, the present research contributes to the dual goals for advanced next-generation energy-storage technologies. First, the research recovers valuable silicon from waste PV panels and, second, the reclaimed silicon is used as an electrode material in Li-ion-based electrochemical systems[29] to promote environmental sustainability in the battery materials supply chain.

In this work, electrode materials were prepared using silicon solar cell waste, and their electrochemical behaviour in Li-ion environments was observed. Moreover, the characteristics of the composite materials on different conducting substrates, such as ITO and graphite sheets, were also examined. In the first step, recycled solar cell scraps are powdered using ball milling to obtain micron-sized particles. The advantages of particles of this size are that they provide a lower specific surface area and greater volumetric capacity. The recycled silicon powder is then treated with NaOH and HCl to remove the impurities. This powder, along with a conductive additive and a binder, forms a composite slurry, which is deposited over different substrates to observe the behaviour of the active silicon material. Different spectroscopic analyses, along with X-ray diffraction spectroscopy (XRD), scanning electron microscopy (SEM), energy-dispersive X-ray spectroscopy (EDAX) and Raman spectroscopy of both the recycled material and the slurry-coated electrode, were performed. Transmission electron microscopy (TEM) of the resulting silicon powder after chemical treatment was performed to investigate the morphology and microstructure of the recycled silicon powder, which provides detailed information about the crystallinity through high-resolution imaging and SAED pattern analysis. Thermogravimetric analysis (TGA) along with differential scanning calorimetry (DSC) and Brunauer–Emmett–Teller (BET) analyses of the chemically treated powder were performed to evaluate the thermal stability, the surface area, and the porosity of the powder, respectively. Atomic force microscopy (AFM) and X-ray photoelectron spectroscopy (XPS) were performed to establish the surface topography and electronic state of the elements present in the recycled powder. In addition to this, electrochemical characterizations, including cyclic voltammetry (CV), electrochemical impedance spectroscopy (EIS) and galvanometric charge–discharge (GCD) analyses were used to characterize the prepared electrodes.

2 Experimental section

2.1 Recycling process of silicon solar modules

The waste silicon solar photovoltaic modules were first disassembled manually to separate the aluminium frames. After the removal of the frames, the waste solar cells attached between the front and back sides of the ethyl vinyl acetate (EVA) layers and the back-sheet were then subjected to thermal treatment at an optimized temperature of 480 °C. This controlled thermal treatment resulted in the effective removal of EVA encapsulation layers, back-sheets and glass fragments, along with the silicon solar cell scraps. The individual silicon solar cell scraps were collected in a Petri dish, then crushed and made into fine powder using a ball milling process at 450 rpm for 6 hours. The resulting fine powder primarily consisted of Si, Ag and Al. This powder sample was then treated with aqueous NaOH solution under continuous stirring.

In this alkaline environment, surface oxides associated with the solar cell waste were partially dissolved by forming soluble sodium silicate, while metallic silicon and other insoluble components remained undissolved.

$$SiO_2(s) + 2NaOH(aq) \rightarrow Na_2SiO_3(aq) + H_2O(l) \quad (1)$$

$$Si(s) + 2NaOH(aq) + H_2O(l) \rightarrow Na_2SiO_3(aq) + 2H_2(g)\uparrow \quad (2)$$

The resulting mixture underwent filtration, and the solid residue that remained on the filter paper was collected. This collected solid material was then subjected to multiple rinses with deionized water (DI water) in order to ensure the removal of any residual soluble sodium-containing compounds.

$$2Al(s) + 2NaOH(aq) + 6H_2O(l) \rightarrow 2Na[Al(OH)_4]^-(aq) + 3H_2(g)\uparrow \quad (3)$$

After the washing procedure, the precipitate was subjected to treatment with HCl solution. This process facilitated the transformation of metallic and other inorganic impurities into their respective chlorides, which enhances their solubility.[30] Along with this, the acidification simultaneously promoted silica formation by precipitating the surplus silicate compounds that were embedded within the solid matrix. This obtained suspension was then subjected to filtration, and the recovered solid was washed repeatedly with DI water to leach out chloride ions. The final product was dried at varied temperatures for further analysis.

$$Na_2SiO_3(aq) + 2HCl(aq) \rightarrow H_2SiO_3(aq) + 2NaCl(aq) \quad (4)$$

$$H_2SiO_3(aq) \rightarrow SiO_2\cdot yH_2O(s) \rightarrow SiO_2 + \text{Water(on drying)} \quad (5)$$

$$2Al(s) + 6HCl(aq) \rightarrow 2AlCl_3(aq) + 3H_2(g)\uparrow \quad (6)$$

$$Na[Al(OH)_4]_{-}(aq) + 4HCl(aq) \rightarrow AlCl_3(aq) + NaCl(aq) + 4H_2O(l) \quad (7)$$

A schematic of the steps involved in the recovery process of silicon and silica powder from waste PV modules and its application in electrode fabrication is shown in Fig. 1.

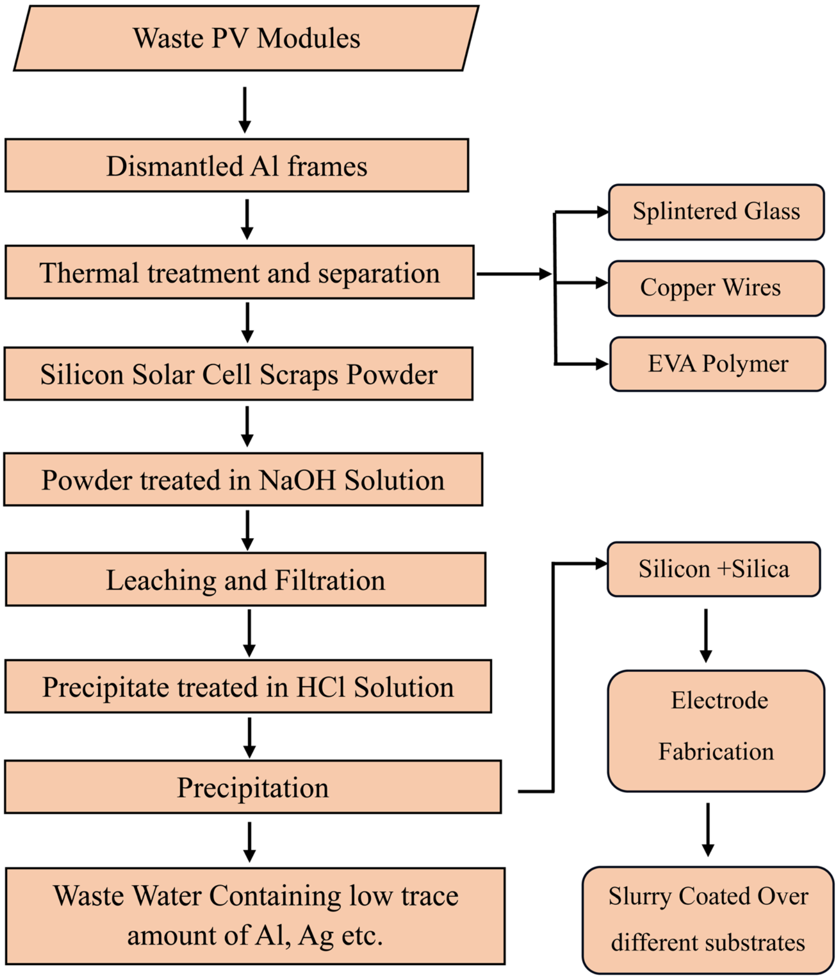

Fig. 1 Flowchart of the recovery process of silicon and silica powder from waste photovoltaic modules and its subsequent application in electrode fabrication.

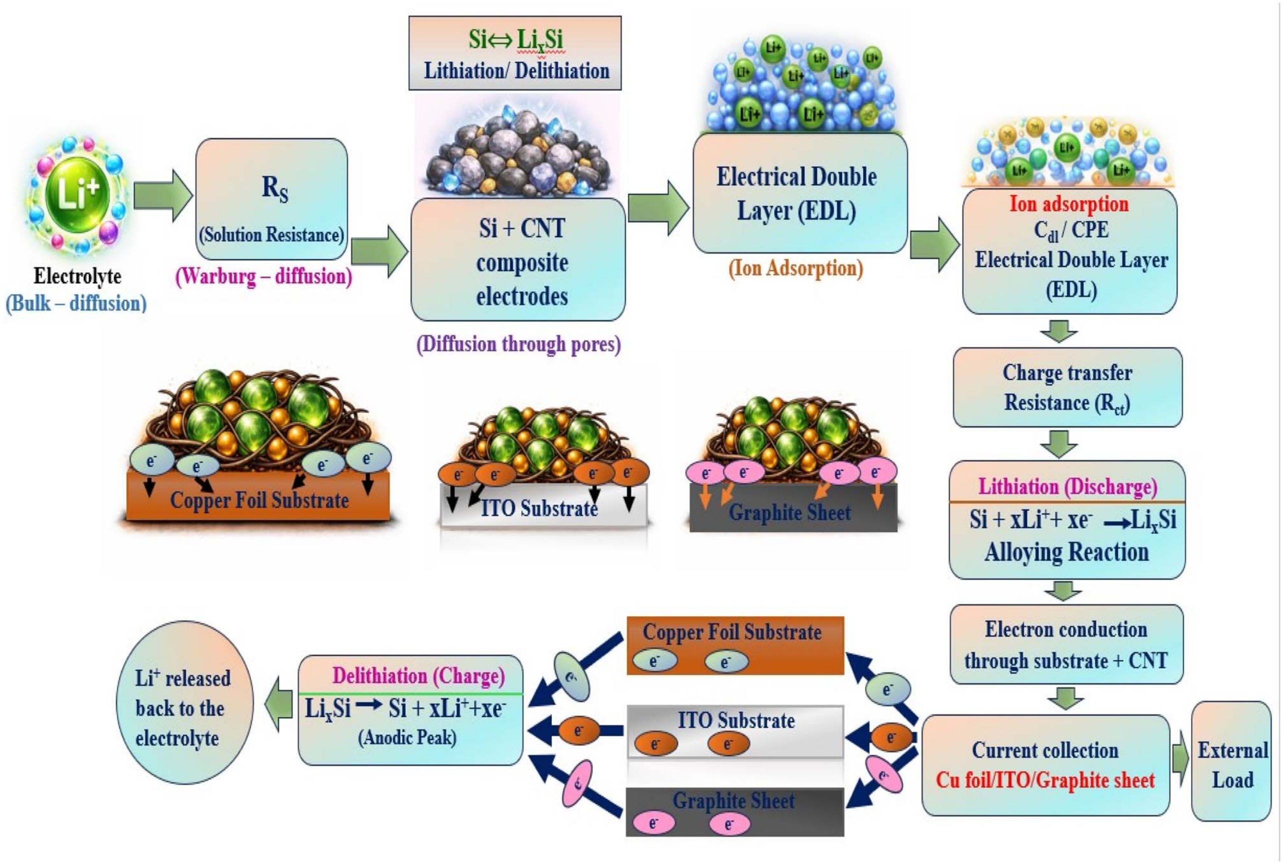

Fig. 2 Flowchart illustrating the charge-transfer process.

2.2 Fabrication of electrodes using the recovered powder as the active material

The chemically recovered powder, which consisted of both Si and SiO_2, was utilized as the essential active material for the electrode fabrication. For the fabrication of the electrodes, the recycled powder was integrated with carbon nanotubes (CNTs), as a conductive additive, polyvinylidene fluoride (PVDF), as the binder, and *N*-methyl-2-pyrrolidone (NMP), as the solvent medium, in a ratio of 80 : 10 : 10 to prepare the slurry. This prepared slurry was then coated over copper foil, ITO and graphite sheet, which acted as current collectors. The coated films over copper foil, ITO and graphite sheet were then dried in a vacuum oven at around 90–100 °C to eradicate excess solvent and facilitate adhesion between the substrate and the binder. The electrochemical performance of the fabricated electrodes was evaluated using the electrolyte composed of 1 M $LiClO_4$ mixed with propylene carbonate (PC). Here, Ag/Ag^+ was used as the reference electrode and Au was used as the counter electrode (Fig. 2).

2.3 Recovery of silicon powder

A cut solar cell module of weight 500 g was put under thermal treatment to obtain solar cell pieces along with glass and copper wires. The solar cell pieces were then separated from other recovered materials and crushed into powder using a ball-milling apparatus at 450 rpm for 6 hours with an interval of 10 minutes. The weight of the crushed solar cell powder was found to be 12.32 g. Out of this quantity of recycled powder, 12 g was taken and divided into 3 batches of 4 g each and then treated with NaOH and HCl in a molar ratio of 1 : 1, 1 : 1.25 and 1 : 1.5, respectively. The recovered silicon powder after the chemical treatment with NaOH and HCl was found to be 3.85 g, 3.91 g and 3.82 g, respectively. Therefore, the highest recovery percentage (about 97.75%) was observed for the 1 : 1.25 molar ratio (Fig. 3). This was estimated based on work done by D. Sah *et al.*[31]

3 Results and discussion

3.1 X-ray diffraction spectroscopy

The X-ray diffraction pattern of the recycled solar cell scraps powder was recorded within the range from 10° to 80° on a 2θ scale using a Rigaku Mini Flex II X-ray diffractometer operating with Cu-K$_\alpha$ radiation of wavelength 1.54 Å (Fig. 4A). A highly intense diffraction peak appeared at $2\theta \approx 28.6°$, which corresponds to the (111) plane of crystalline silicon. This intense peak appeared primarily due to the diamond cubic crystal structure of silicon, which confirmed the retention of its crystalline form during the recycling process. The additional peaks located at angles 47.5°, 56.2°, 69.2° and 76.5° were assigned to the (220), (311), (400) and (331) planes, respectively, which

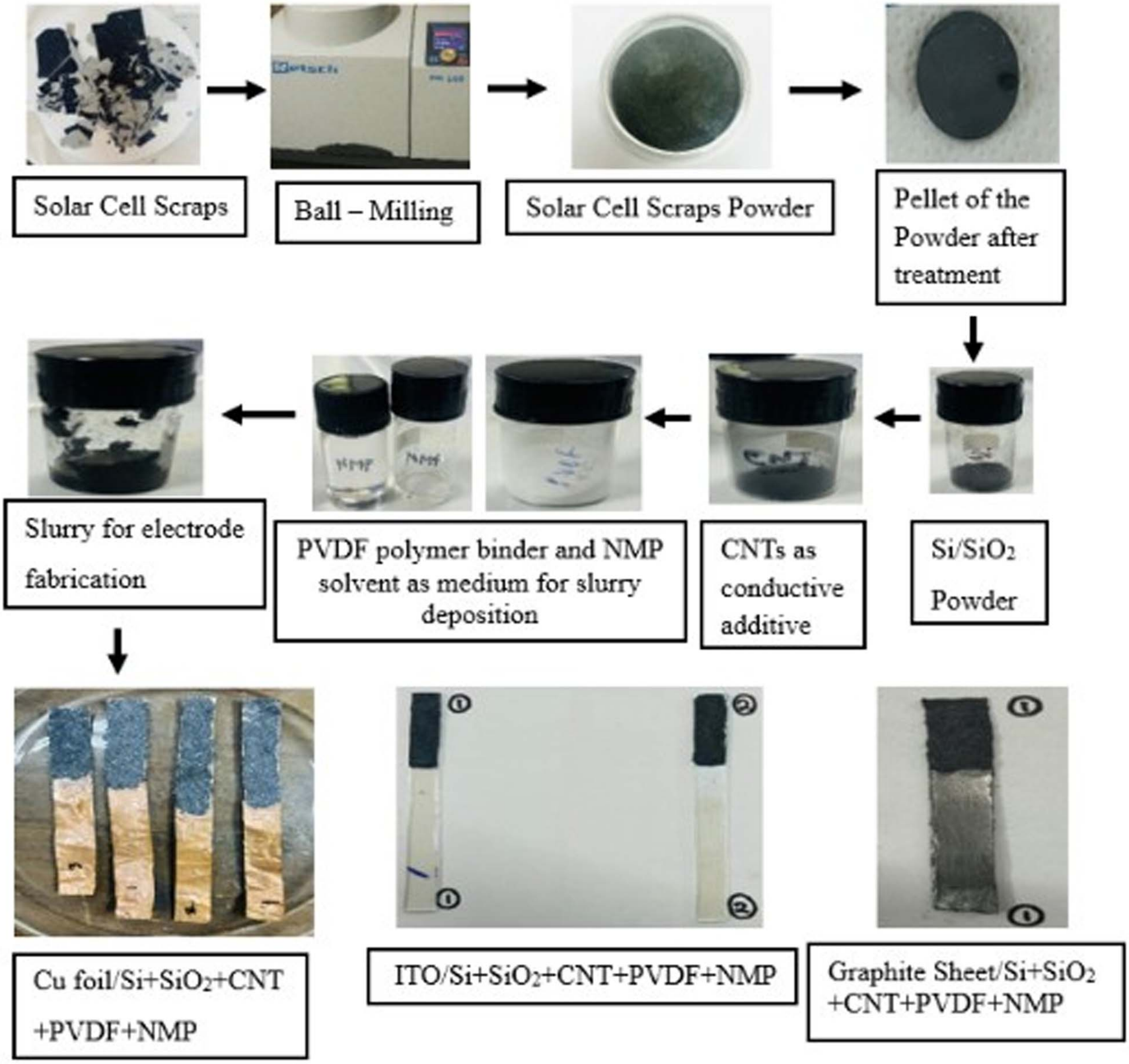

Fig. 3 Complete steps for the fabrication of electrodes using recycled silicon solar cell powder.

further confirms the presence of crystalline silicon. The X-ray diffraction pattern also provides evidence for the presence of metallic residues such as aluminium (Al) and silver (Ag). The diffraction peaks appearing at $2\theta \approx 38.6°$, $2\theta \approx 65.1°$ and $2\theta \approx 78.3°$ were attributed to the (111), (220) and (311) planes of aluminium, respectively, which originate from the back-contact layer of the silicon solar cell. The only peak of silver (Ag) was observed in this X-ray diffraction pattern at around $2\theta \approx 44.8°$, which was indexed to the (200) plane and comes from the front metal grid of the silicon solar cell.

The crystalline properties of the recovered powder, obtained from the solar cell scraps after consecutive treatment with NaOH and HCl, were examined using X-ray diffraction (XRD) techniques. The diffraction pattern, as shown in Fig. 4B, displayed sharp and well-defined diffraction peaks, which confirms the presence of multiple crystalline phases within the recycled powder sample. The major diffraction peaks observed at around $2\theta \approx 28.4°$, 47.3°, 56.1°, 69.1° and 76.2°, corresponding to the (111), (220), (311), (400) and (331) crystal planes of silicon, respectively. Apart from the silicon peaks, an additional peak at around 26.6° corresponds to the (102) plane of silicon dioxide (SiO_2), indicating that the silicon surfaces experienced partial oxidation during the chemical treatment process. The presence of SiO_2 is because the interaction with aqueous environments generally facilitates the formation of thin oxide layers over the silicon particles. Thus, the X-ray diffraction patterns confirmed that the recycled powder mainly consists of crystalline silicon, along with small contributions from silicon oxide (SiO_2). The co-existence of crystalline silicon along with a minor secondary phase like SiO_2

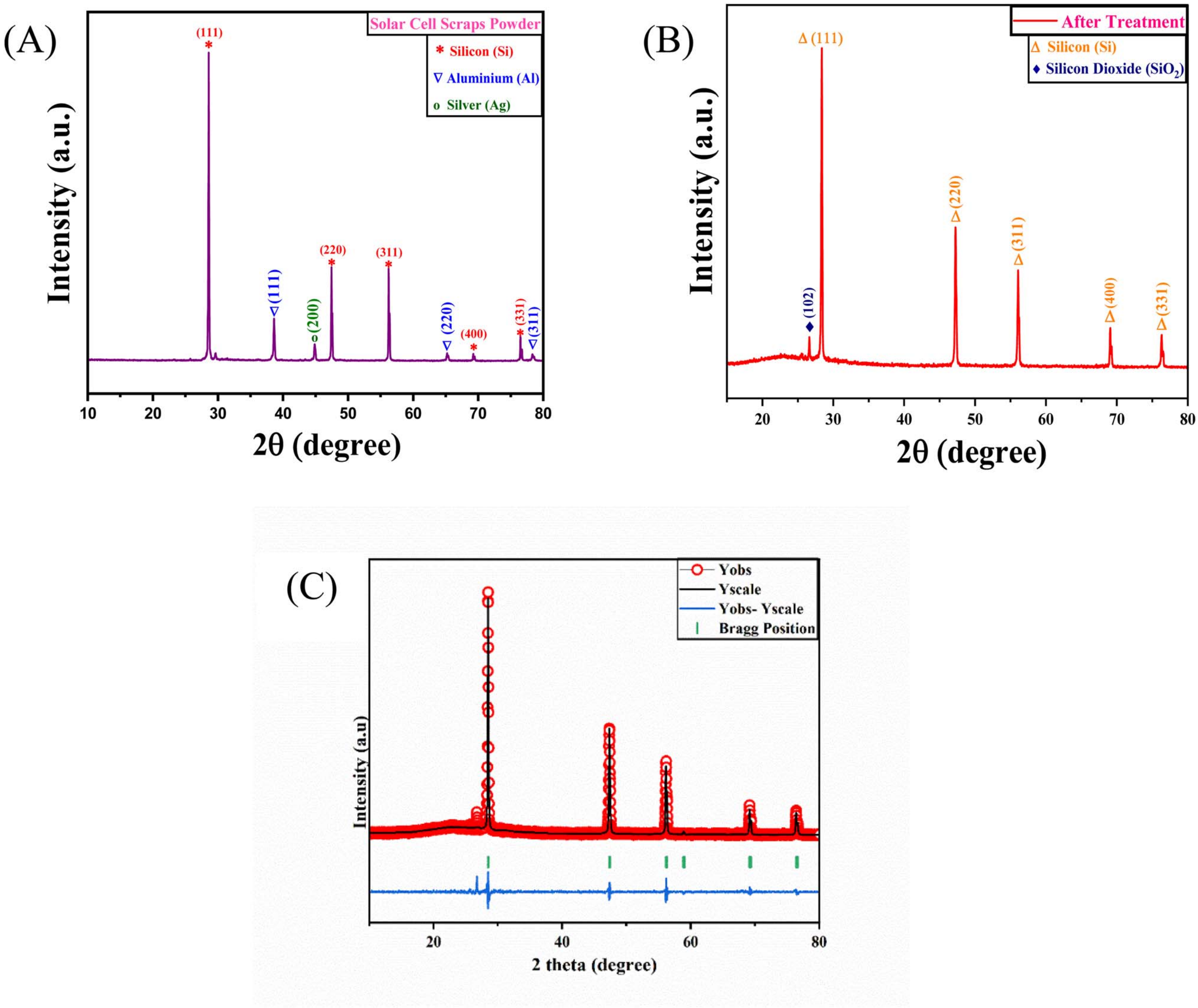

Fig. 4 XRD plots of the recycled solar cell scraps powder (A) before chemical treatment and (B) after chemical treatment. The powder sample without chemical treatment exhibits characteristic diffraction peaks of crystalline silicon along with the impurity phases of aluminium (Al) and silver (Ag). The XRD pattern of the powder sample after chemical treatment in (B) is primarily composed of silicon peaks along with the presence of silicon dioxide (SiO_2) due to the partial oxidation, while the elimination of impurities confirms the efficiency of the treatment. (C) Rietveld refinement of the X-ray diffraction pattern of chemically treated recycled silicon powder. The experimentally observed intensities in red circles are in good agreement with the calculated patterns, shown as black solid lines, indicating good quality fitting. The vertical green lines represent the Bragg reflection positions corresponding to the crystalline silicon.

demonstrates the efficient recovery of silicon (Si) through the chemical treatment, which is consistent with the standard JCPDS card no. 00-027-1402. The high-intensity peak corresponding to the (111) plane shows the preferred orientation of the recovered and successfully separated silicon and its preserved crystalline nature.

The crystallinity index (CI) of the prepared silicon powder sample after chemical treatment was found to be 48% from its XRD plot. Furthermore, to determine the concentration of Si in the crystallite growth, we calculated the crystallite size and lattice strain produced in the lattice using the well-known Williamson–Hall equation:

$$\beta \ \mathrm{Cos} \ \theta = \frac{K\lambda}{D} + 4\varepsilon \ \sin \ \theta \tag{8}$$

where β is the FWHM that corresponds to each peak in the XRD data measured in radians, θ is the diffraction angle in radians, K is the shape factor (considered to be equal to 0.9 for our sample), λ is the wavelength of the X-rays (Cu K_α source in our case), D is the crystallite size, and ε is the lattice strain.

The crystallite size D is calculated to be 67.28 nm, and the lattice strain ε is found to be 9.28×10^{-4} from the Williamson–Hall equation.

Table 1 Rietveld refinement details of the recycled silicon powder sample after chemical treatment

R_p	R_{wp}	R_{ep}	χ^2	$a = b = c$ (Å)
35.8	25.8	12.99	3.93	5.426

The Rietveld refinement analysis of the chemically treated recycled silicon powder was performed, and the parameters are represented in Table 1.

3.2 FESEM-EDAX analysis

Fig. 5 shows a cross-sectional field-emission scanning electron microscopy (FESEM) image of a crystalline silicon solar module, which illustrates its multilayer structure. The glass was removed from the sample used for cross-sectional FESEM. As clearly labelled in the micrographs below, the back-sheet, subsequent EVA encapsulant, core silicon wafers, and a second EVA layer are arranged sequentially from bottom to top. The sheet protects the inner layers from external stress, while the EVA acts as an encapsulant as well as protective and optical coupling material. They securely hold the silicon wafers within them, where energy conversion occurs.

To understand the surface morphology and distribution of impurities in the crushed powder sample, it was characterized through the field-emission scanning electron microscopy (FESEM) and energy-dispersive X-ray spectroscopy (EDAX). Fig. 6A displays a heterogeneous mixture of non-uniform particle morphology with irregular geometries, which is due to the crushing and material breakdown process during recycling. The microstructure consists of a combination of fine small grains along with larger thin sheet-like particles, which indicates the presence of silicon-abundant domains as well as the residual surface layers.

The EDAX spectrum in Fig. S1A and EDAX data in Fig. 6B confirm that the recovered silicon solar cell scraps powder sample was composed of silicon (Si), which is nearly 71.09% by weight and 65.88% by atomic percentage. The second major component present in the powder sample is aluminium, with a weight percentage of 19.04% and an atomic percentage of 18.37%. The 9.64% weight percentage and 15.69% atomic percentage of oxygen highlight the presence of oxide phases that can be associated with either silicon or aluminium. In addition, the presence of a very small amount of silver (0.22 weight% and 0.05 atomic%) indicates trace metallic residues originating from the front contact electrodes. No hazardous elements such as lead (Pb) were observed in the EDAX data.[32] Therefore, it can be concluded from these data that the recycled powder is primarily composed of crystalline silicon with metallic impurities such as Ag and Al, which come from the electrode and back contact layers.

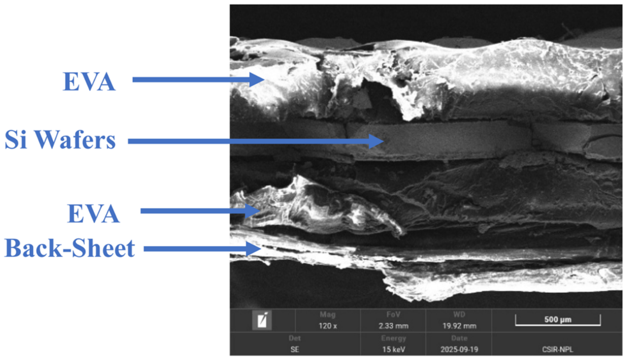

Fig. 5 Cross-sectional FESEM image of a crystalline silicon solar module after removal of the glass, highlighting the presence of the silicon wafer pieces within the front and back EVA layers along with the back-sheet layer beneath it.

The crushed silicon solar cell powder was treated with NaOH and the precipitate collected from this process was treated with HCl. The FESEM image in Fig. 6C shows the presence of unevenly shaped and non-uniform particles with etched and irregular surfaces. The treatment with NaOH efficiently etched the silicon, resulting in micro-sized grains with fine particles. Following this step, the chemical reaction with HCl produces a mixture of silicon flakes and finer particles. The presence of surface roughness is observed because of the SiO_2 content. Fig. S1B shows the EDAX spectrum and Fig. 6D shows the EDAX data, which highlights the changes that occur in the elemental composition after the two-step chemical treatment process. From the EDAX data, it is observed that the treated powder consists of 53.76 wt% silicon, along with contributing 67.09 at% of the total detected elements. The noticeable quantity of oxygen is either due to the formation of a SiO_2 layer, which arises because of the HCl-induced precipitation, from the sodium silicate formed during the alkaline treatment, or due to the oxidation of the etched silicon surfaces. A negligible amount of Al (~1.69 wt%) is detected, which is primarily from the back contact of the silicon solar cell during the recycling process. As compared to the EDAX data of the powder before chemical treatment, the Ag impurities are removed after the chemical treatment process. Therefore, the SEM microstructural image and the EDAX data confirm that this recycling process produces a Si/SiO_2 powder. This surface texture and oxide presence will help in providing better performance in electrode fabrication.

3.3 Raman spectroscopy analysis

Fig. 7A shows the Raman spectrum of the recycled silicon solar cell scraps powder after chemical treatment with NaOH and HCl. The spectrum exhibits a distinct and intense peak at around 516 cm^{-1}, which signifies the first-order optical phonon vibration mode of crystalline silicon. This strong and distinct peak indicates that the recycled powder retains mainly its crystalline nature after the chemical treatment processes. The spectrum also shows a small band at around 295 cm^{-1} that corresponds to the higher-order phonon interactions in silicon.[33] In addition to this, a broad peak near 960 cm^{-1} relates to the Si–O stretching, which indicates the partial surface oxidation of silicon because of the chemical treatment. After the chemical treatment process, the recovered powder was subjected to high-temperature annealing at 1500 °C in a vacuum tube furnace under an inert atmosphere, and the Raman

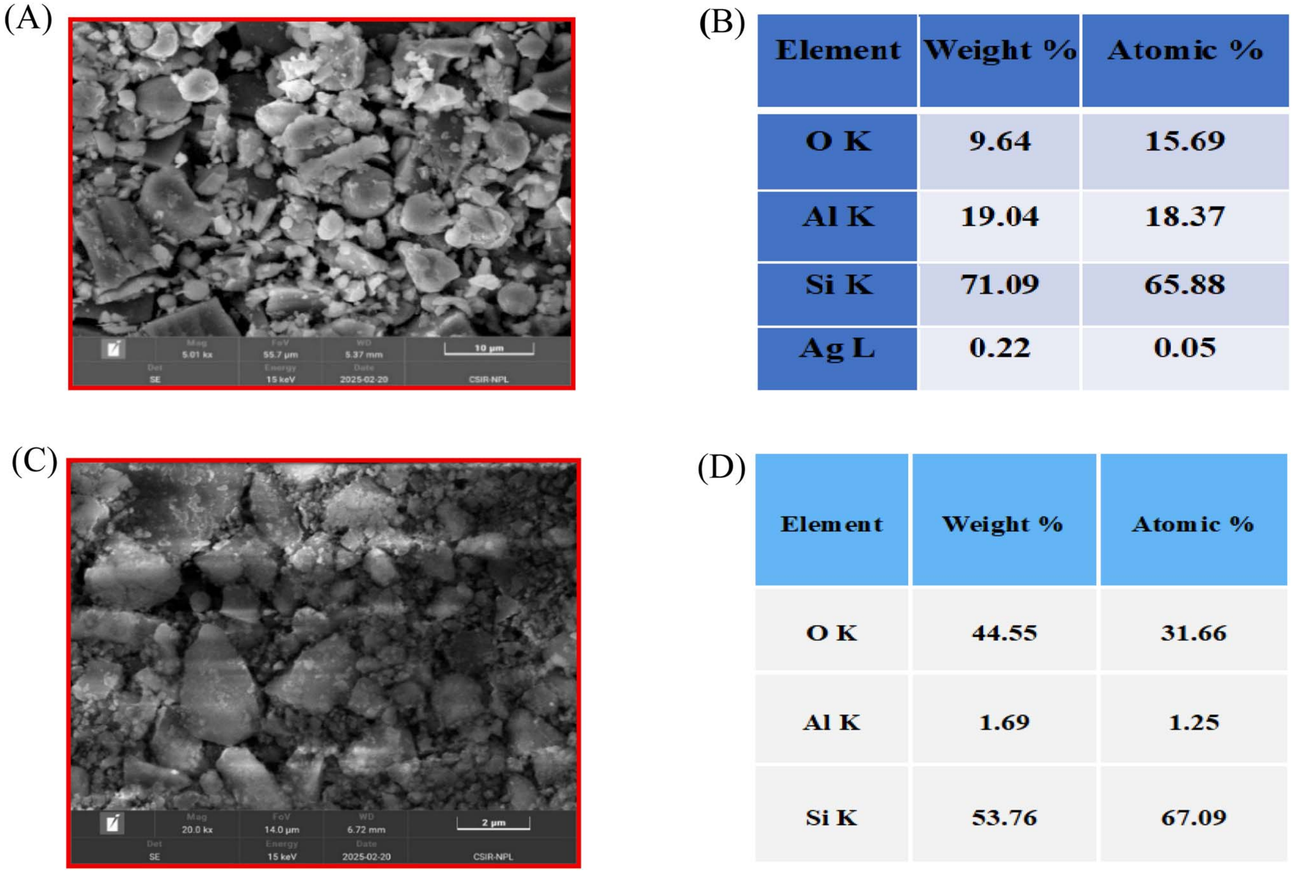

Element	Weight %	Atomic %
O K	9.64	15.69
Al K	19.04	18.37
Si K	71.09	65.88
Ag L	0.22	0.05

Element	Weight %	Atomic %
O K	44.55	31.66
Al K	1.69	1.25
Si K	53.76	67.09

Fig. 6 (A) FESEM image of crushed silicon solar cell scraps powder before chemical treatment, showing irregularly shaped agglomerated particles and non-uniform surface morphology, and the (B) corresponding EDAX analysis, confirming the presence of silicon as the primary element, along with appreciable content of Al and O, along with traces of Ag. (C) FESEM image of the chemically treated solar cell scraps powder displaying a cleaner surface morphology along with reduced agglomeration, suggesting the removal of impurities, and the (D) corresponding EDAX analysis, indicating a reduction in the wt% of Si and Al along with a higher content of O formation due to the presence of SiO_2 after the chemical treatment.

spectrum of this powder is shown in Fig. 7B. This spectrum exhibits a sharp and intense peak at around 524 cm^{-1}, which again shows the characteristic feature of the first-order optical phonon mode of crystalline silicon. This post annealed Raman spectra shows a more intense and slightly shifted peak, which signifies better crystallinity and reduction in crystal defects. The weaker band at around 307 cm^{-1} remains present, which corresponds to the higher-order phonon interactions in silicon. Moreover, a broad band at around 963 cm^{-1} originates from Si–O stretching vibrations, signifying a small contribution from oxide phases. These results confirm that the vacuum furnace annealing improves the crystallinity of the recycled silicon powder, which increases its suitability for electrode fabrication.

3.4 X-ray photoelectron spectroscopy analysis

Fig. 8 shows the X-ray photoelectron spectroscopy plot, which was used to investigate the chemical composition and electronic states of the silicon 2p core of the recycled powder. This spectrum produces distinct peaks for both elemental silicon (Si) and silicon dioxide (SiO_2), which confirms the existence of both species within the chemically treated sample. Here, as shown in Fig. 8, two characteristic doublets were observed in the spectrum, which signifies the spin–orbit coupling of the Si 2p core level electrons. The lower binding energy peaks at around 99.0 eV to 100.0 eV correspond to the Si $2p_{3/2}$ and Si $2p_{1/2}$ states of crystalline silicon, and the peaks corresponding to higher binding energy at approximately 103.0 eV to 104.0 eV indicate the Si $2p_{3/2}$ and Si $2p_{1/2}$ states of oxidized silicon, representing the +4 oxidation state of silicon.[34] The presence of these silicon oxide peaks highlights the surface oxidation of the recycled silicon in the chemical treatment process. The fitted curve (in red), denoted as the peak sum, matches closely with the experimentally determined intensity spectrum.

The high intensity of the oxide-related peaks suggests that a substantial portion of the powder surface is oxidized. The existence of both Si and SiO_2 peaks indicates that the chemical treatments using NaOH and HCl partially remove native surface oxide but also enhance oxidation, producing a composite of both elemental Si and SiO_2.

3.5 Atomic force microscopy image analysis

The surface topography of the recycled silicon solar cell scraps powder after the chemical treatment with NaOH and HCl was studied by atomic force microscopy (AFM). The images reveal

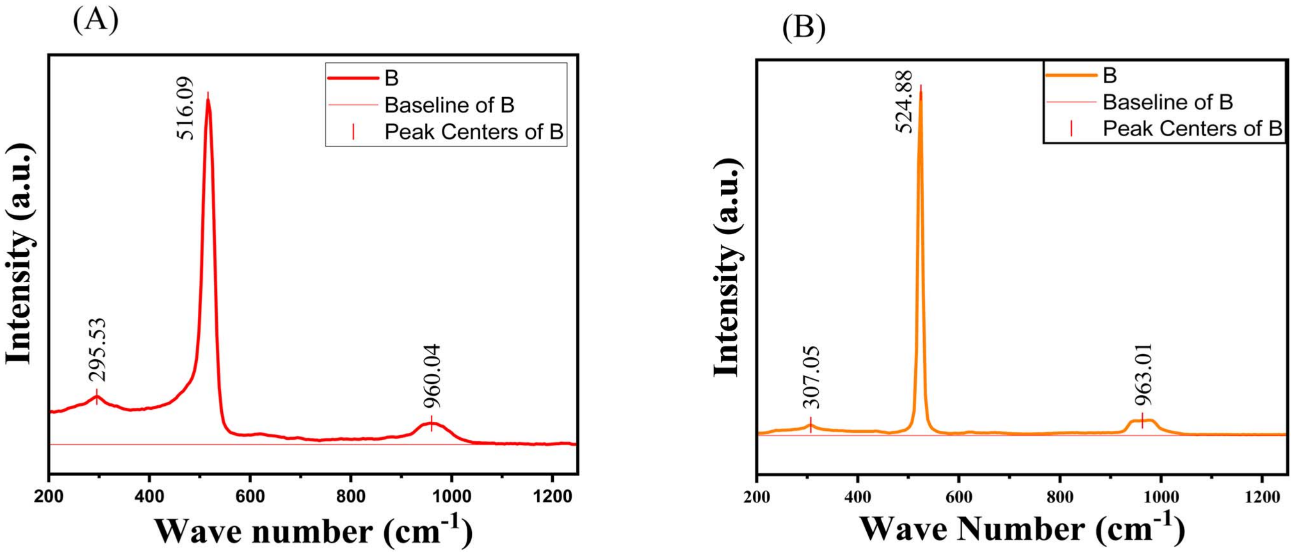

Fig. 7 Raman spectra of recycled silicon powder (A) before annealing, showing a broadened Si peak at ∼516.09 cm^{-1} signifying structural disorder and phonon confinement effects, and (B) after annealing, highlighting a sharper and more intense peak at ∼524.8 cm^{-1} along with reduced broadening, which confirms the enhancement in crystallinity and defect reduction.

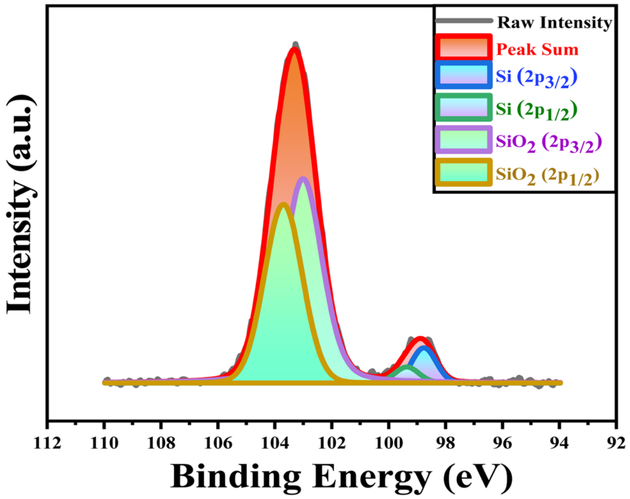

Fig. 8 X-ray photoelectron spectra of the chemically treated silicon powder, showing the deconvoluted Si 2p region. The raw intensity (in black) and fitted peak sum (in red) are highlighted along with the peaks of the individual components corresponding to elemental silicon (Si 2p$_{3/2}$ and Si 2p$_{1/2}$) and oxidized silicon contributions (SiO$_2$ 2p$_{3/2}$ and SiO$_2$ 2p$_{1/2}$). The spectrum is dominated by Si 2p contributions, confirming the presence of elemental silicon, whereas the presence of SiO$_2$-related components indicates the partial surface oxidation of the recovered powder.

a heterogeneous surface consisting of densely packed fine particles present across the whole mapped surface. The height of the scale bar indicates a broad vertical profile, which shows the presence of both small granules and large agglomerated particles after the chemical treatment of the powder sample.[35] The surface morphology shows the presence of both brighter and darker regions composed of silicon and silicon oxide containing particles due to the removal of surface layers during chemical etching. The existence of sharp rises and deep depressions results in a highly distinct rough nano-scale surface, which is good for lithium-ion storage as it facilitates electrolyte penetration and improves charge-transfer kinetics across the electrode–electrolyte interface (Fig. 9).

3.6 Transmission electron microscopy and SAED pattern analysis

The microstructures of the recycled silicon powder after chemical treatment were analysed using transmission electron microscopy. The bright-field TEM image in Fig. 10A shows irregular sheet-like structures with sizes within the sub-micron range, indicating the aggregation of finer particles. The corresponding high-resolution TEM image shown in Fig. 10B exhibits distinct lattice fringes that confirm the crystalline nature of the silicon. The limited irregularity and discontinuity in the crystal planes suggest the formation of structural defects during the chemical treatment process. In addition, the selected area electron diffraction (SAED) pattern, as shown in Fig. 10C, showcases prominent concentric rings with bright spots as the characteristics of a polycrystalline structure. The diffraction rings correspond to various crystallographic planes of silicon, further confirming the retention of crystallinity after treatment. The observed diffraction rings were analysed to determine the corresponding interplanar spacings (*d*-spacing values) in Fig. 10D. The prominent diffraction rings are indexed to the characteristic planes of silicon, namely (111), (220), (311) and (400), respectively.

3.7 X-ray fluorescence spectroscopy analysis

Quantitative analysis of the recovered silicon powder was carried out with a wavelength dispersive X-ray fluorescence spectrometer (WD-XRF; ElvaX spectrometer) using a helium target to check the purity of the sample. This quantitative

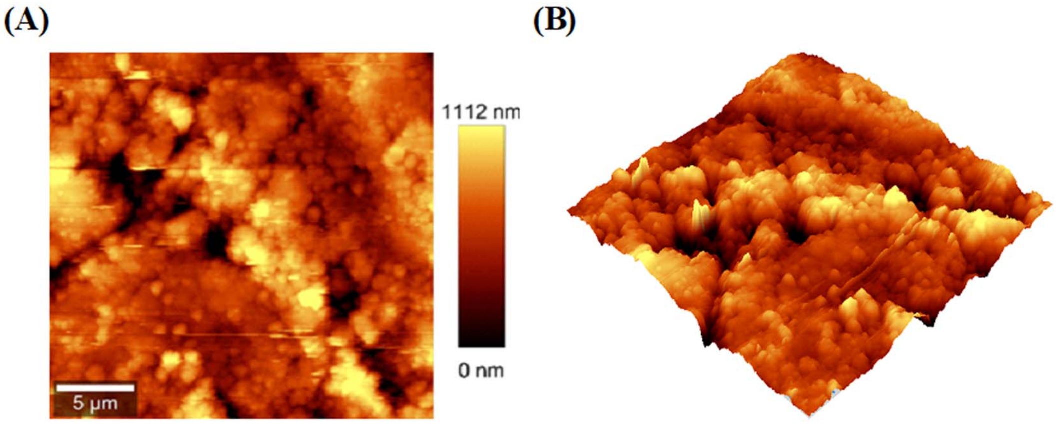

Fig. 9 AFM image analysis of recycled silicon powder after chemical treatment. (A) 2D-image illustrating the surface morphology, revealing agglomerated particle features with distinct surface roughness. The height of the surface varies up to 1112 nm. (B) 3D topographical image showing the surface texture and height distribution, confirming the presence of irregularly distributed clusters.

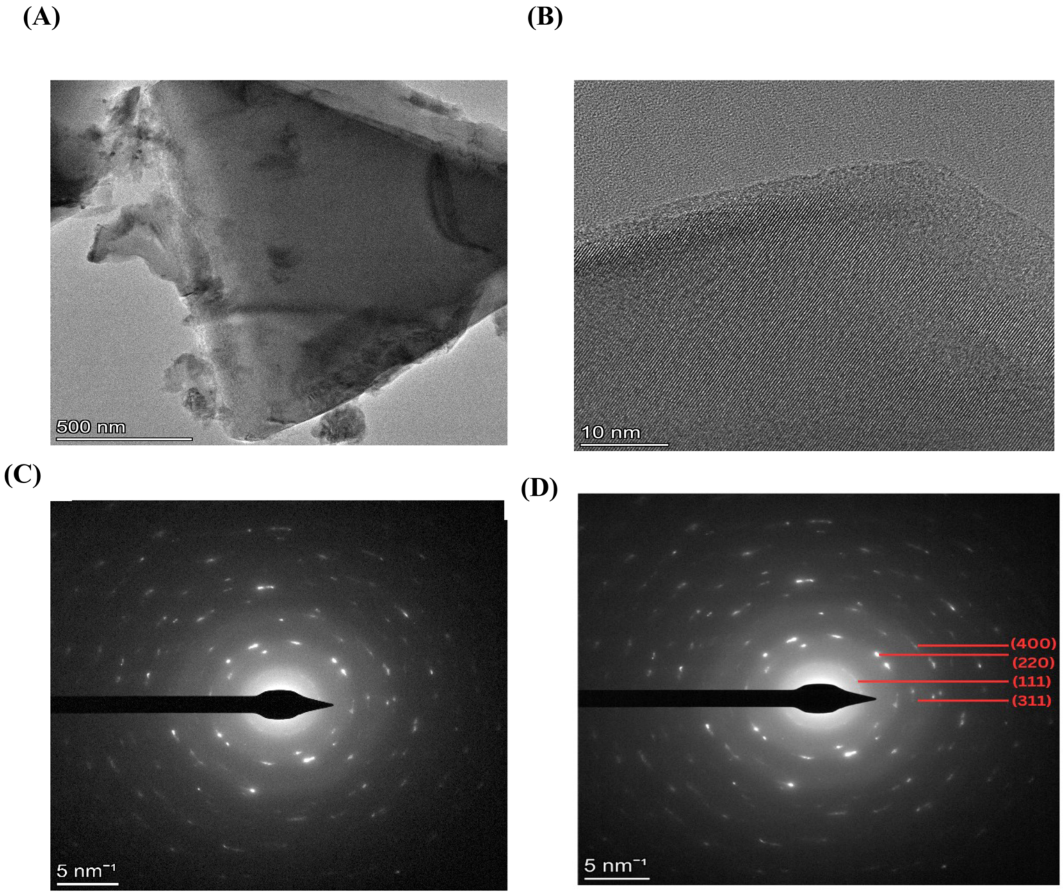

Fig. 10 Transmission electron microscopy images of the prepared recycled silicon powder after chemical treatment: (A) bright-field TEM image highlighting agglomerated and irregularly shaped silicon particles with dimensions in the sub-micron range. (B) High-resolution TEM image revealing the presence of noticeable lattice fringes that confirm the crystalline nature of the silicon. (C) Selected area electron diffraction (SAED) pattern exhibiting the presence of diffraction rings with bright spots, indicative of a polycrystalline structure. (D) Indexed SAED pattern where the diffraction rings are assigned to the (111), (220), (311), and (400) crystallographic planes of crystalline silicon, based on analysis of the calculated *d*-spacing.

analysis of the sample as characterized through XRF is shown in Fig. S2A. The X-ray fluorescence spectrum shows a major silicon peak with maximum intensity and a concentration of 99.52%. Along with silicon, other elemental impurities such as Fe, Ca, Cr, V, Ti, S, and Mn are detected. The extremely low concentrations of Cu, Ag and other remaining elements imply that these impurities have a negligible impact on the purity of the material.[36] Fig. S2B shows the X-ray fluorescence intensity spectrum, in which Si-K$_\alpha$ is the major peak. Furthermore, the other peaks of Fe, Ca and Ag have comparatively much smaller intensities, and the absence of any other additional strong peaks confirmed that no other major phases are present in the recovered silicon powder. Hence, the XRF results indicate that the recovery process produces silicon with a purity of 99.52%, with minimal impurities. The observed purity reflects the efficient recovery of silicon from waste solar panels and confirms the suitability of the material for the preparation of electrodes.

3.8 BET surface area analysis

The BET (Brunauer–Emmett–Teller) analysis of the recycled silicon powder after chemical treatment was performed to calculate the pore structure and the surface properties of the powder. The analysis is based on both the desorption and adsorption plots. The desorption plot shows a gradual increase in the cumulative pore volume with increasing pore diameter, whereas the pore size distribution dV(d) exhibits a higher contribution from smaller pores, indicating the formation of a mesoporous structure. Similarly, in the case of the adsorption plot, the cumulative pore volume increases progressively with increasing pore diameter, along with the significant presence of

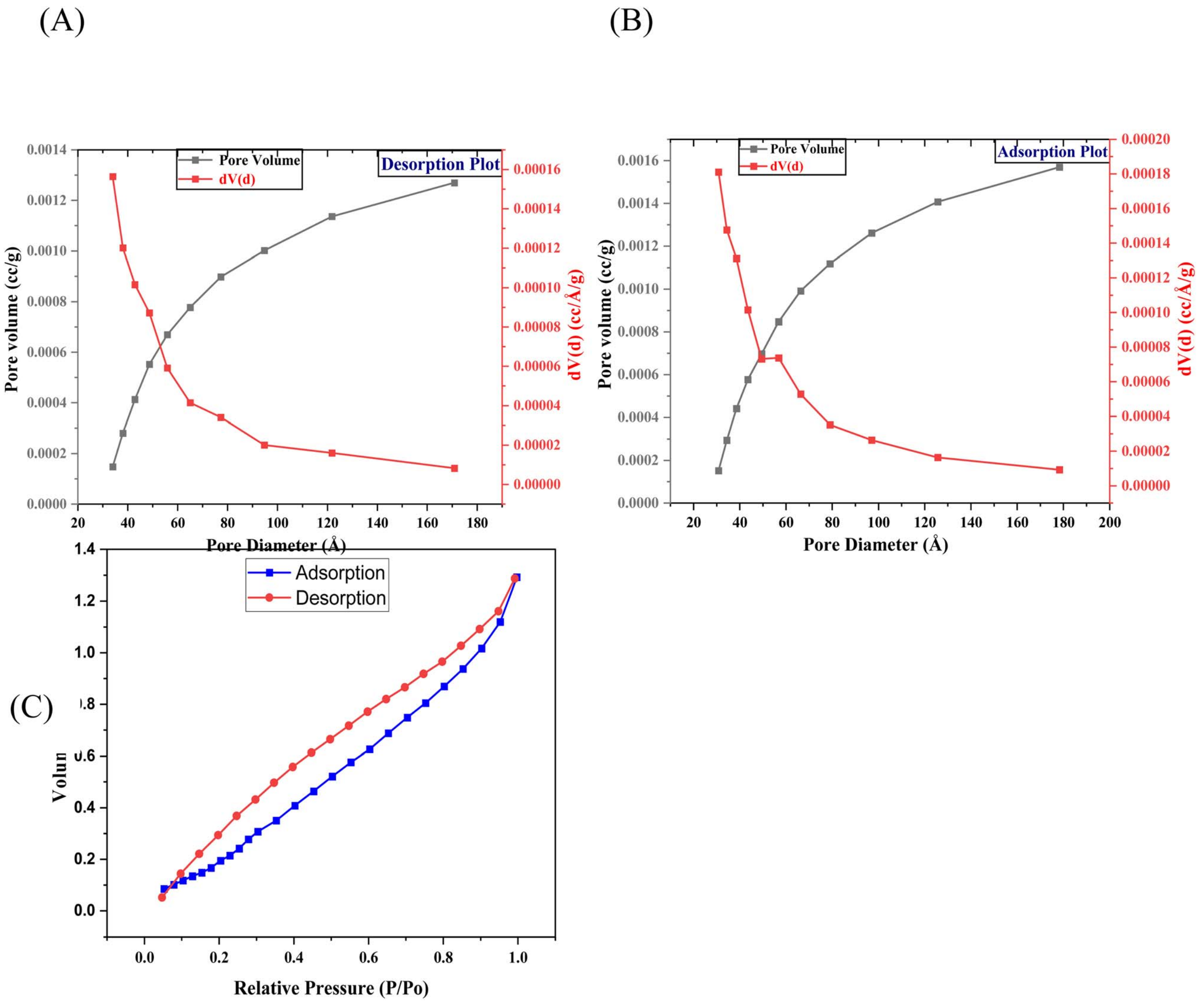

Fig. 11 (A) BET desorption results of the recycled silicon powder after chemical treatment, highlighting the variation in cumulative pore volume and pore-size distribution with pore diameter. This plot describes the increase in pore volume along with a larger contribution from smaller pores by suggesting the formation of a moderate mesoporous structure. (B) BET pore structure analysis from the adsorption plot of the recycled silicon powder prepared after chemical treatment. The plot shows the increase in cumulative pore volume with pore diameter, whereas the pore-size distribution curve reveals a higher density of smaller pores, which also confirms the presence of a porous structure after chemical treatment. (C) Nitrogen adsorption–desorption isotherm of the chemically treated recycled silicon powder measured from the BET analysis. The volume of nitrogen adsorbed (cc g^{-1}) is plotted against relative pressure (P/P_0), which shows a continuous increase in adsorption along with the increase in relative pressure. The occurrence of a small hysteresis between the adsorption and desorption curves indicates the presence of mesoporosity. The observed shape of this isotherm exhibits the characteristics of Type IV behaviour, describing the formation of a mesoporous structure after the chemical treatment.

smaller pores. The close agreement between the desorption and adsorption curves shows the formation of a mesoporous structure in the chemically treated recycled silicon powder.

The nitrogen desorption and adsorption isotherm of the chemically treated recycled silicon powder, as shown in Fig. 11C, illustrates a gradual increase in adsorbed volume with increasing relative pressure (P/P_0), which reflects a continuous pore-filling process across the complete relative pressure range. The adsorption and desorption curves form a hysteresis loop, which is the characteristic of mesoporous structures associated with condensation within narrow pores.

At low relative pressure values, the gradual enhancement in adsorption reflects the low content of micro-pores as well as the initial surface adsorption, whereas the increased adsorption at higher relative pressures indicates multilayer adsorption within mesoporous structures. The isotherm describes the Type IV plot, which shows the characteristics of mesoporous materials by confirming the development of porous structure after chemical treatment. The small separation between adsorption and desorption curves shows appreciable pore connectivity, which is also favourable for ion transport. The surface area of the powder sample from the BET analysis is found to be 1.544 $m^2 g^{-1}$.

3.9 Thermogravimetric and differential scanning calorimetry analyses

TGA-DSC analysis of the recycled silicon powder exhibits negligible variation in weight throughout the temperature range up to 800 °C. The nearly constant TGA curve, which is ~100%, highlights minimal weight loss, reflecting high thermal stability and negligible volatile content. A very small reduction in the initial weight observed at temperatures below 200 °C can be attributed to the removal of residual solvents trapped within the structure of the recycled silicon powder. A slight increase in weight at higher temperatures of ~200 °C to 600 °C is likely due to the gradual surface oxidation of silicon under trace oxygen conditions. The DSC curve illustrates a weak endothermic feature in the initial temperature region, which is again due to desorption of moisture or relaxation of surface-bound species. A distinct exothermic peak is observed, which is associated with structural rearrangement within the silicon matrix (Fig. 12).

4 Characterizations of the fabricated electrodes

4.1 X-ray diffraction spectroscopy. Fig. 13A illustrates the X-ray diffraction plot of the electrode made over copper foil, obtained within the range from 10° to 90° on the 2θ scale. The most intense diffraction peak was observed at $2\theta \approx 47.18°$, which corresponds to the (220) plane of crystalline silicon. This indicates that the highly ordered crystal arrangement of silicon is predominantly oriented along that direction. Other diffraction peaks located at 28.5°, 56.14°, 69.14°, 76.32° and 87.94° are assigned to the (111), (220), (400), (331) and (422) planes, respectively, which further confirms the presence of crystalline silicon. This shows that silicon is an active material that plays the key role in the electrode. Apart from these diffracted peaks of silicon, two other peaks, observed at around $2\theta \approx 43.22°$ and $2\theta \approx 50.26°$, represent the (111) plane and (200) plane of the

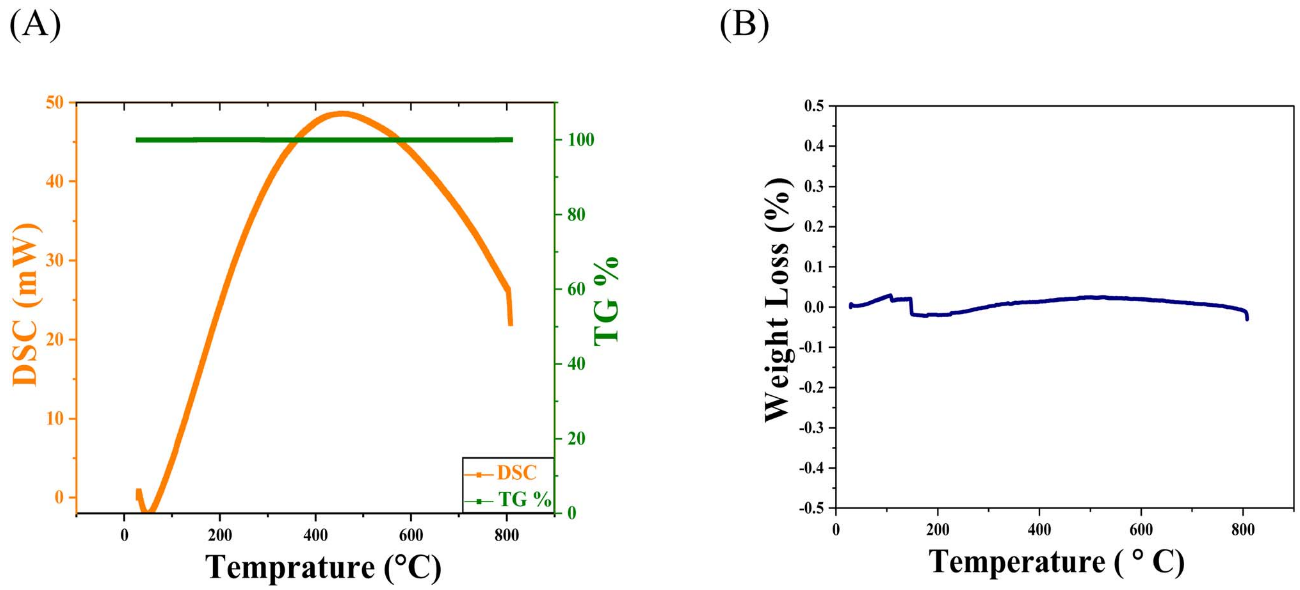

Fig. 12 (A) Thermogravimetric analysis (TGA) and differential scanning calorimetry (DSC) plots of chemically treated recycled silicon powder recorded up to 800 °C. The TG% curve, showing negligible weight loss (~0.03%), indicates high thermal stability and effective removal of volatile impurities after chemical treatment. The presence of a broad endothermic DSC curve highlights the absence of significant thermal degradation as well as any exothermic reactions. (B) Thermogravimetric analysis (TGA) curve of the prepared recycled silicon powder after chemical treatment, showing negligible variation in weight loss percentage (~±0.04%) up to 800 °C, which indicates high thermal stability and minimal presence of the heat-sensitive substances. A minimal change in weight (~0.02–0.03%) below 200 °C is because of the evaporation of adsorbed moisture along with loosely bound surface species, followed by a nearly completely stable region, with a slight increase in weight between 200 °C and 600 °C. The weight remains constant with slight fluctuations at higher temperatures, which confirms the absence of significant thermal decomposition.

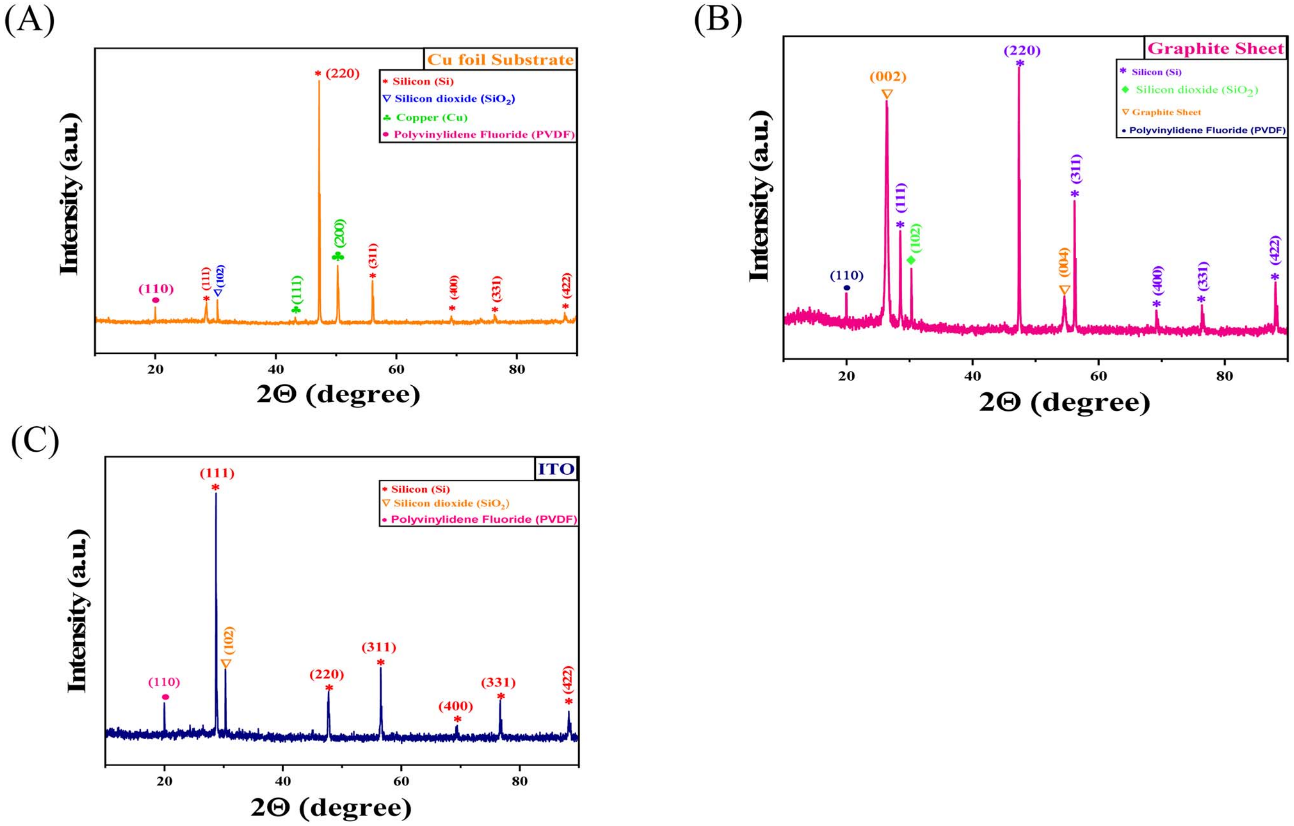

Fig. 13 XRD plots of the Si/SiO_2 composite electrode fabricated over different substrates: (A) copper foil, (B) graphite sheet, and (C) ITO substrate. The presence of the diffraction peaks corresponding to the planes (111), (220), (311), (400), and (331) of the crystalline silicon is observed in all cases. The existence of SiO_2 indicates partial oxidation of the material. In addition to this, distinct peaks of the copper substrate are present in (A), whereas a strong peak at ~26° in (B) corresponds to the (002) plane of the graphite; in the case of ITO, no such peaks from the substrate are observed. The presence of peaks from the binder is also observed for all the substrates.

crystalline copper substrate, respectively, which is present below the electrode film. A polymer, polyvinylidene fluoride (PVDF), was used as a binder during the preparation of the electrode to increase adhesion of active material with the substrate; therefore, a minor peak at around $2\theta \approx 20.0°$ is observed, which corresponds to the (110) plane of the crystalline α-phase of PVDF. In addition, a small diffraction peak was observed around $2\theta \approx 30.30°$, which relates to the (102) plane of silicon dioxide (SiO_2). This peak reveals that a small amount of silicon was partially oxidized at the surface.

The X-ray diffraction plot of the electrode prepared from recycled silicon as active material over the graphite sheet, observed within the range from 10° to 90° on the 2θ scale, is shown in Fig. 13B. The most intense diffraction peak was observed at $2\theta \approx 47.36°$, which corresponds to the (220) plane of crystalline silicon. The other diffraction peaks observed at 28.54°, 56.18°, 69.18°, 76.4° and 88.08° were assigned to the (111), (220), (311), (400), (331) and (422) planes, respectively. These planes confirm the presence of crystalline silicon. Other than the presence of active material silicon, a diffraction peak at 30.3° corresponds to the (102) plane of silicon dioxide. Furthermore, the presence of two peaks observed at around $2\theta \approx 26.38°$ and $2\theta \approx 54.58°$ indicates the (002) and (004) planes of the substrate graphite sheet. The XRD pattern also contains a very small peak at around $2\theta \approx 20.0°$, similar to that of the Cu foil substrate, which describes the (110) plane of crystalline PVDF.[37]

The Fig. 13C shows the X-ray diffraction plot of the electrode over the ITO substrate, observed within the range from $2\theta \approx 10°$ to $2\theta \approx 90.0°$. Similar to that of the slurry deposited over the other two substrates, the XRD peak at $2\theta \approx 20°$ indicates the (110) plane of crystalline PVDF. In addition, the peak at $2\theta \approx 30.3°$ highlights the presence of the (102) plane of SiO_2. The most intense peak was observed at $2\theta \approx 28.72°$, which indicates the (111) plane of crystalline silicon. The maximum intensity peak corresponding to the (111) plane differs from that of the most intense peak of Si in the case of the other two substrates, which might be because of factors such as deposited film thickness, difference in preferred crystallographic orientation, or substrate diffraction. The other diffraction peaks observed at 47.68°, 56.54°, 69.46°, 76.72° and 88.3° correspond to the (220), (311), (400), (331) and (422) planes of crystalline silicon, respectively.

4.2 SEM-EDAX analysis

The micro-structures of the composite electrodes prepared by depositing the silicon composite over copper foil, ITO and graphite sheet were characterized using field emission scanning

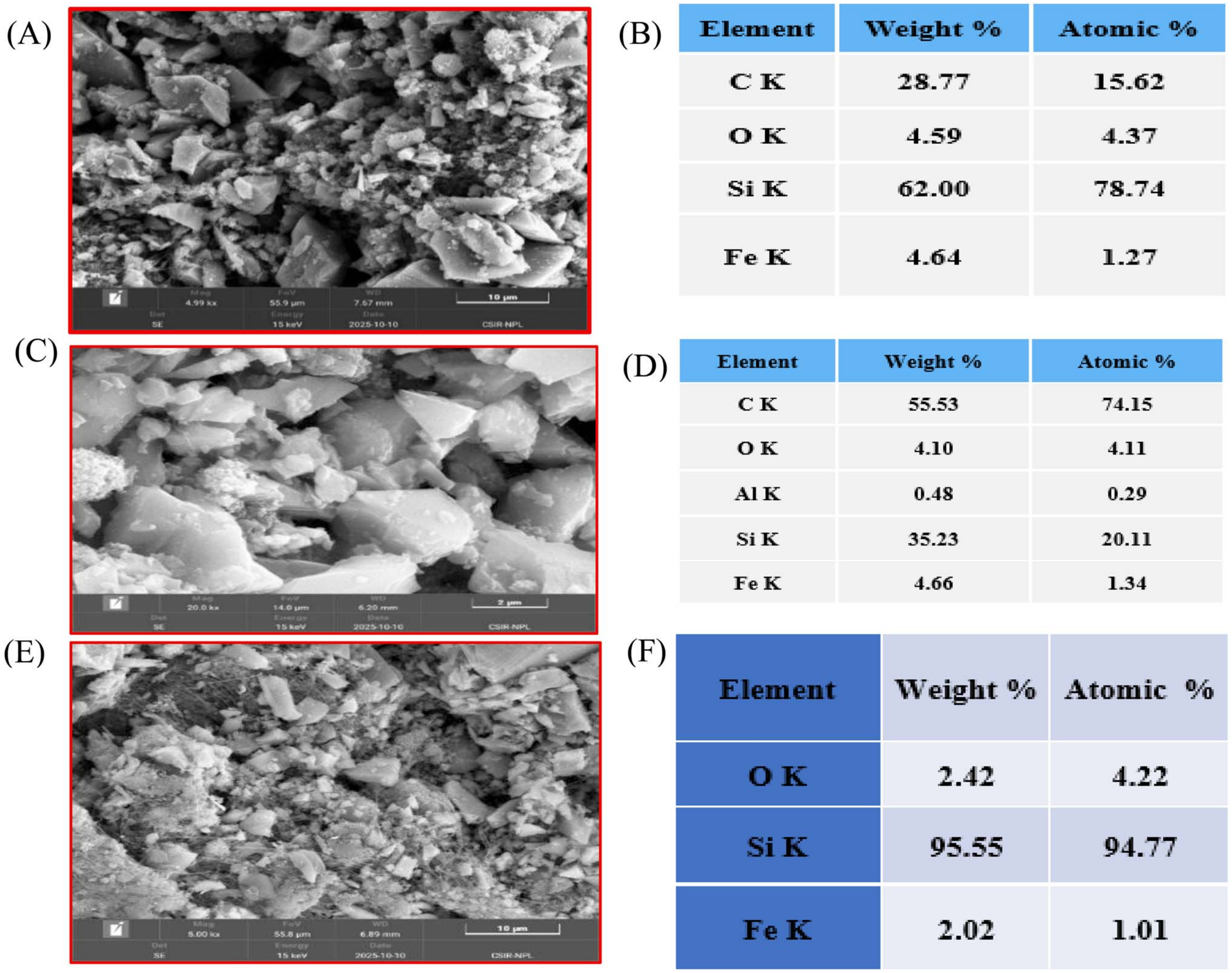

(B)

Element	Weight %	Atomic %
C K	28.77	15.62
O K	4.59	4.37
Si K	62.00	78.74
Fe K	4.64	1.27

(D)

Element	Weight %	Atomic %
C K	55.53	74.15
O K	4.10	4.11
Al K	0.48	0.29
Si K	35.23	20.11
Fe K	4.66	1.34

(F)

Element	Weight %	Atomic %
O K	2.42	4.22
Si K	95.55	94.77
Fe K	2.02	1.01

Fig. 14 (A) FESEM image of the silicon-based composite electrode prepared over a Cu foil, showing aggregated particles with a heterogeneous morphology and non-uniform spatial distribution, with the (B) corresponding EDAX analysis displaying Si as the major wt% element along with contributions from C, O and minor traces of Fe. (C) FESEM image of the slurry-coated ITO substrate electrode showing a more uniform and compact particle arrangement, and the (D) corresponding EDAX data, indicating an increase in the content of carbon as a conductive additive. (E) FESEM image of the electrode made over a graphite sheet, showing uniformly distributed particles with reduced agglomeration and improved surface uniformity, and the (F) corresponding EDAX results confirming the presence of a higher content of Si along with a reduction in the oxygen and impurity wt%.

electron microscopy (FESEM). The FESEM micrograph obtained for the electrodes made over copper foil (Fig. 14A) exhibits a rough and non-homogeneous surface identified by randomly distributed particles with flake-like segments. This composite electrode morphology consists of closely packed irregular grains along with fine particles forming a compact network arrangement. The tightly packed configuration minimizes void formation by strengthening the intimate conductive pathway or charge transport network across the Si/SiO_2 and conductive carbon nanotube network. Fig. 14B confirms the elemental composition of the coated slurry. The major silicon peak, as shown in Fig. S3A with 62.00 wt% and 78.74 atomic%, highlights that silicon constitutes the primary portion of the electrode, and the prepared electrode surface is mainly Si-rich. The second major component present in the electrode slurry is carbon, with a weight percentage of 28.77% and an atomic percentage of 15.62%, which mainly comes from the CNTs. A minor peak of Fe, with 4.64 wt% and 1.27 atomic%, signifies the presence of residual iron (Fe) catalyst particles originating from the carbon nanotube synthesis process, as iron is often employed as a catalyst during CNT functionalization.

The FESEM image of the silicon composite slurry-coated ITO substrate is shown in Fig. 14C. The surface morphology of this electrode exhibits larger and more angular domains with sharp edges along with intense contrast, which corresponds to the crushed silicon pieces from the recycled silicon solar cells. As shown in Fig. 14C, the silicon particles appear densely packed in some regions, whereas in other regions these particles are surrounded by uniformly distributed fine particles originating from the surface oxidation of silicon. The aggregation of smaller particles attached to the silicon grains shows the presence of SiO_2, and the thin, elongated string-like structures are the CNTs embedded within the silicon grains. The low contrast regions that appear in the image correspond to the PVDF binder that holds the silicon and CNT firmly over the ITO substrate. The EDAX data in Fig. 14D indicate that the major contribution comes from silicon, which is approximately 55.53 wt% and 74.15 at%. A considerable amount of carbon (approximately 35.23 wt%) is present, which is due to the CNTs added as a conductive additive. A small content of oxygen (∼4.10 wt%) and Fe (∼4.66 wt%) shows the presence of surface oxide and traces of Fe used as a catalyst during the synthesis of the CNTs. A negligible amount of aluminium (∼∼0.48 wt%) is also observed. The EDAX spectrum shown in Fig. S3B describes a sharp peak corresponding to silicon, confirming that the main component in the recovered powder is silicon. In addition to this, minor peaks corresponding to C, Fe, and O, and a very small peak corresponding to Al, are also present, which indicate the presence of surface impurities.[38]

From the FESEM image in Fig. 14E, the surface morphology of the slurry-coated graphite sheet substrate shows that the deposited slurry forms a surface composed mainly of large, angular, crystalline silicon particles originating from the crushed silicon wafers. These larger crystalline silicon flakes were surrounded by smaller, fine and irregular particles, which correspond to surface SiO_2 formed because of the chemical treatment. The regions with low contrast highlight the presence of PVDF, which acts as a binder that occupies the voids and holds the silicon and SiO_2 particles firmly over the graphite substrate. This can facilitate the diffusion of the electrolyte during the electrochemical cycling process. The energy-dispersive X-ray spectrum and elemental composition of this electrode are shown in Fig. S3C and 14F. The dominant silicon peak corresponds to around 95.55 wt% and 94.77 atomic%, along with a very small content of oxygen arising from surface oxide. A very small peak of Fe, with 2.02 wt% and 1.01 atomic%, indicates the presence of residual iron catalyst particles associated with the CNT synthesis process.

Thus, the collective FESEM–EDAX results show that the electrode slurry is mainly composed of silicon, with a minor oxide content and is uniformly integrated within the CNT-PVDF network over the graphite sheet substrate.

4.3 Raman spectroscopy analysis

The Raman spectrum of the silicon composite slurry deposited on copper foil is shown in Fig. 15A. This spectrum reflects the distinct vibrational bands corresponding to the different structural constituents of the electrode. The strongest peak occurs at ∼514.72 cm^{-1}, which indicates the first-order optical phonon mode of crystalline silicon. The high intensity of this peak signifies that the recycled silicon mainly conserves its

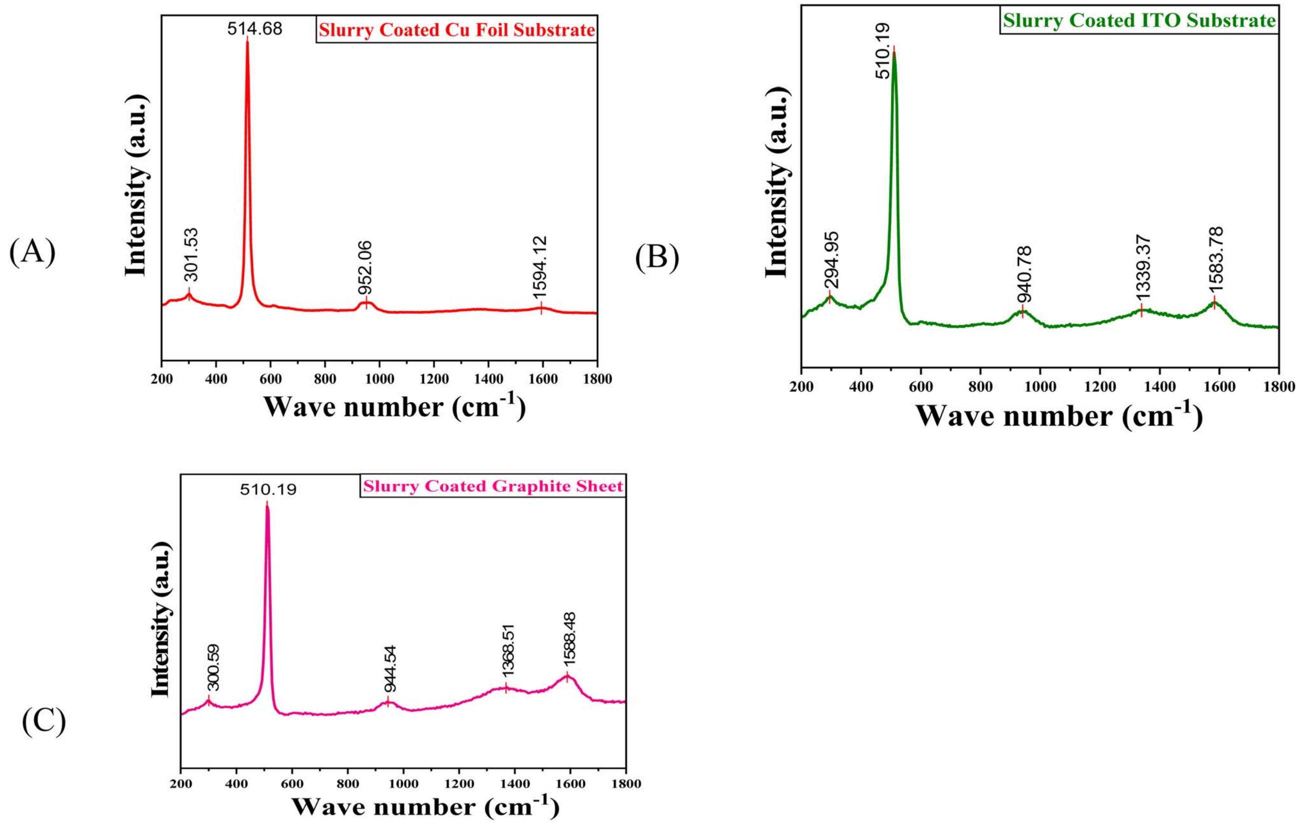

Fig. 15 Raman spectra of slurry deposited electrodes over (A) Cu foil, (B) ITO, and (C) graphite sheet. In all three spectra, the characteristic vibrational bands of the active material silicon are observed. The spectrum recorded for (A) Cu foil exhibits a prominent peak with reduced background intensities, indicating good coating over the substrate. (B) For ITO, additional low-intensity bands are found because of the conductive oxide layer, and (C) for graphite sheets, the spectrum displays broader peaks along with the increased background intensity due to the graphite substrate and its interaction with the coated layer.

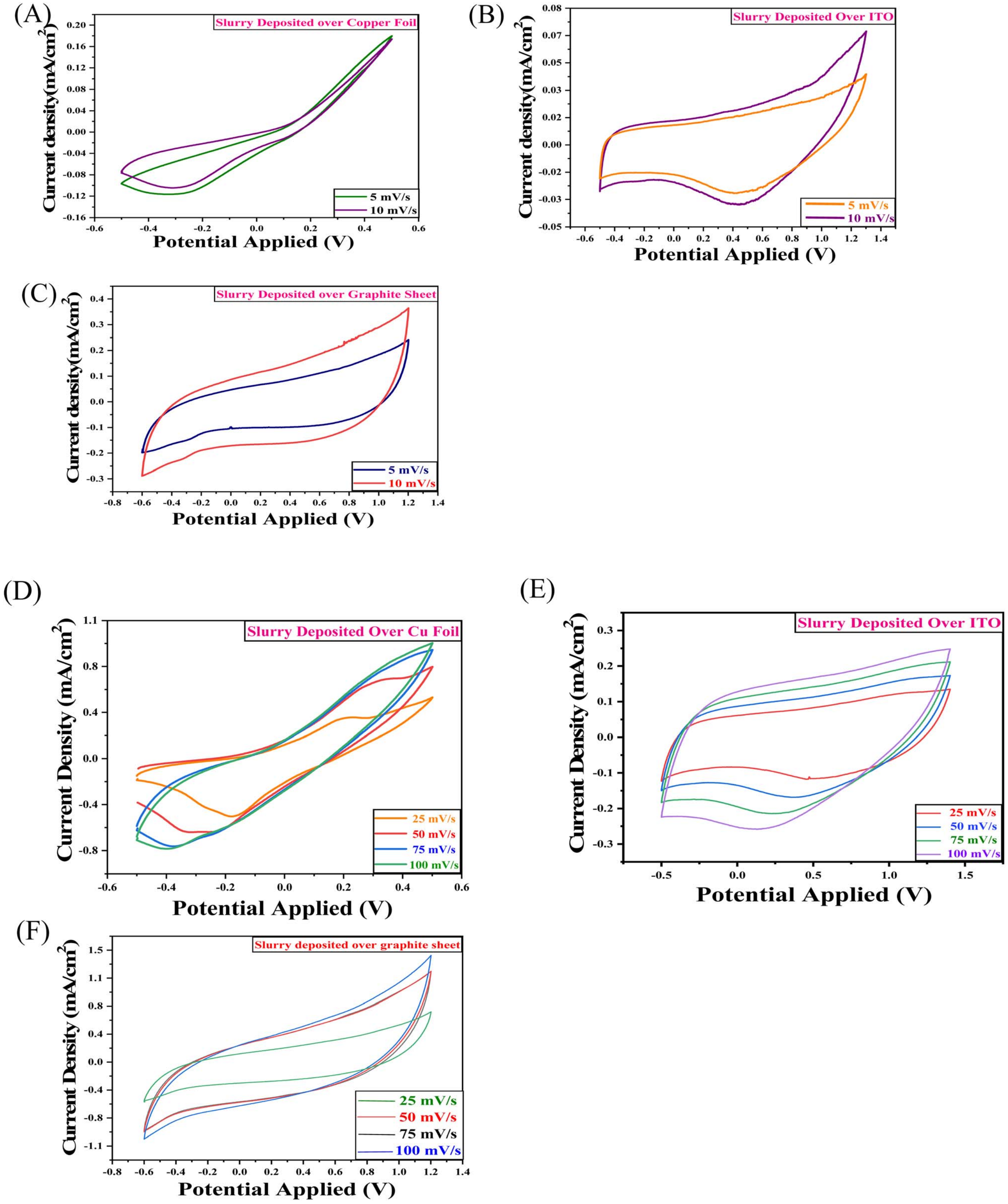

Fig. 16 CV curves of slurry-coated electrode over three different substrates (A) Cu foil, (B) ITO, and (C) graphite sheet, measured at the scan rates of 5 mVs^{-1} and 10 mVs^{-1}. The plot in (A) shows a quasi-rectangular shape, suggesting the co-existence of a faradaic process and the double-layer capacitance over the Cu foil electrode. In (B), the curves display increased current response along with redox behavior, indicating improved electrochemical activity due to the ITO substrate. The CV curves in (C) show wider loop areas and appreciable shapes that reflect better charge-storage behavior as well as effective interaction between the active material and the graphite sheet substrate. CV curves of slurry-coated electrode over three different substrates: (D) Cu foil, (E) ITO, and (F) graphite sheet, obtained at the scan rates ranging from 25 mVs^{-1} to 100 mVs^{-1}. The plot in (D) shows well-defined cathodic and anodic peaks at the lower scan rates (25 mVs^{-1} and 50 mVs^{-1}), indicating the occurrence of lithiation and de-lithiation of silicon, along with the shifting and broadening of peaks with increased scan rate. In the case of (E), expansion of the CV curves with the increment in scan rate is observed, and the retention of the

crystalline nature even after the deposition of the slurry over the substrate. A weak band observed at ∼301.26 cm^{-1} might be because of the higher-order phonon scattering process resulting from surface defects. A broad band observed around 951.77 cm^{-1} highlights the presence of Si–O–Si or Si–OH vibrations, which occurred because of the formation of a native oxide layer over the surface of the silicon. This also shows that silicon is the key Raman active material, although the presence of SiO_2 is observed. Other than the active-material-related modes, a peak at around 1595 cm^{-1} highlights the presence of the G-band of carbon, originating from the carbon nanotubes added as a conductive additive to the slurry.

Fig. 15B shows the Raman spectrum of the electrode prepared by depositing the silicon composite slurry over the ITO substrate. Among the different vibrational bands, the highest and most intense peak is observed at ∼510 cm^{-1}, which corresponds to the characteristics of the primary optical phonon vibrations of crystalline silicon. This downshift behaviour from that of the bulk silicon is because of the strain within the silicon particles. The weaker intensity band observed at ∼294.95 cm^{-1} signifies the secondary and defect-linked silicon vibrations, which are associated with the heterogeneous silicon domains. A small and broad peak detected at ∼940.78 cm^{-1} indicates the Si–O–Si stretching band, which is formed during the recycling process.

The two broad peaks featured at ∼1339.37 cm^{-1} and ∼1583.78 cm^{-1} represent the D-band and G-band of carbon, respectively, describing the co-existence of both defect-linked disorder and the ordered nature due to the sp^2 network, which are characteristics of CNTs.[39] The Raman vibrational spectrum of the slurry deposited over the graphite sheet shows different characteristic vibrational modes related to silicon, silicon oxide and carbon-based components, as shown in Fig. 15C. The most dominant peak appears at ∼510.19 cm^{-1}, which is due to the fundamental optical phonon vibration associated with crystalline silicon. The shift of this peak signifies the occurrence of lattice strain and phonon confinement inside the lattice. Although a downshift in the peak occurred, the intensity showcases the crystalline nature of the silicon in the heterogeneous mixture. In this case, a weaker peak is also observed at ∼300.58 cm^{-1}, which is linked to defect-activated secondary silicon vibrations. Again, a moderate intensity peak at around ∼945 cm^{-1} represents the stretching vibrations between silicon and oxygen, which supports the existence of oxide within the composite material. The two broad bands shown in the figure at ∼1369 cm^{-1} and ∼1588 cm^{-1} correspond to the D- and G-bands of carbon, which highlight the characteristic disordered and ordered domains of carbon nanotubes.

4.4 Cyclic voltammetry analysis

Fig. 16D highlights the cyclic voltammetry (CV) curves of the electrodes prepared over the copper foil, analysed at different scan rates of 25 mV s^{-1}, 50 mV s^{-1}, 75 mV s^{-1} and 100 mV s^{-1} within the potential range from −0.6 V to +0.6 V. The CV curve analysed at the scan rate of 25 mV s^{-1} exhibits a nearly symmetric loop with well-defined anodic and cathodic peaks at +0.1786 V and −0.1582 V, respectively. The cathodic peak corresponds to the lithiation process of silicon and the formation of Li_xSi phases. During the anodic potential sweep, the broad anodic peak is observed at +0.178 V, which describes the de-lithiation process of Li_xSi with the partial reformation of silicon. The nearly symmetric cathodic and anodic behaviour, along with the potential difference of ∼0.336 V, shows negligible polarization and appreciable electrochemical reversibility, which confirms the effective charge transport and lithium-ion diffusion across the surface of the electrode. The conductive CNT network enhances the electron movement during electrochemical cycling, whereas the silicon and silicon oxide domains facilitate Li^+ insertion and extraction. At a scan rate of 50 mV s^{-1}, the cathodic and anodic peaks remain distinguishable with a slight shift towards −0.23 V and +0.32 V, respectively. This shift indicates a minimal increase in polarization and diffusion resistance at higher scan rates due to the insufficient time available for the Li^+ transport compared to that at 25 mV s^{-1}. The presence of well-defined peaks confirms that the lithiation and de-lithiation process remains reasonably reversible, which signifies appreciable electrochemical performance and suitability for battery-type energy-storage applications. The incomplete loop is primarily due to the higher polarization, which indicates that the electrochemical response of the prepared electrode is sensitive to the scan rate, and an ideal rate of potential change is required to maintain a balance between diffusion of lithium ions and a reduction of side reactions. With an increase in the scan rate to 75 mV s^{-1}, the cyclic voltammetry curve becomes nearly symmetrical but exhibits broader curves reflecting the co-existence of both faradaic and capacitive type charge storage behaviour. In this curve, the cathodic peak is observed near −0.36 V, which indicates lithiation of silicon and the Li_xSi alloy formation. The weak anodic peak in this curve describes incomplete de-lithiation because of slow diffusion of Li^+ ions across the silicon–electrolyte interface or the presence of a residual SEI (solid–electrolyte interface) layer formed in the lithiation process.[40,41] At a higher scan rate of 100 mV s^{-1}, the cyclic voltammetry curves show broad and less distinct anodic peaks with an increased gap in the potential between the peaks. The cathodic peak is detected at −0.376 V, whereas the anodic peak is flat and weak, which indicates a rise in polarization and a slower charge-transfer rate. The reduced anodic current density at this higher scan rate is due to the incomplete de-lithiation of Li_xSi phases, along with increased charge transfer resistance and high capacitive effects that suppress the contribution from faradaic processes.

The cyclic voltammetry curves of the electrodes made from a slurry containing recycled silicon as active material deposited over ITO substrates, observed at various scan rates of 25 mV s^{-1}, 50 mV s^{-1}, 75 mV s^{-1} and 100 mV s^{-1} within the applied

actual shape of the curve at higher scan rates indicates efficient electrochemical activity over the ITO. The plots in (F) exhibit nearly symmetric and progressively broader loops with increasing scan rate, which reflects a capacitive process along with an appreciable interfacial charge transfer.

potential range from −0.5 V to +1.5 V is shown in the Fig. 16E. At the scan rate of 25 mV s^{-1}, the CV curves show the smallest currents and narrowest area under the curve. In comparison to higher scan rates, the forward and reverse cycles are very close in this scan rate, which indicates that the slower scan rate allows more complete surface redox reactions and reduced polarization. The broad cathodic and anodic peaks at this scan rate represent the near-equilibrium state, where both the diffusion-controlled reactions and the slower faradaic reaction process contribute significantly to the current-density response. When the scan rate is increased to 50 mV s^{-1}, the applied potential range becomes wider, and the maximum current density value increases to +0.16 mA cm^{-2}. The cyclic voltammetry curve spreads out more, which suggests an improved capacitive behaviour with the increase in the scan rate. The maximum anodic current density occurs around 1.4 V, whereas the cathodic peak current density occurs around −0.5 V, which indicates a steady and stable electrochemical behaviour of the electrode. At the scan rate of 75 mV s^{-1}, the magnitude of the current density increases to the maximum value of +0.20 mA cm^{-2}, with the CV curve spreading outward prominently. The broadest CV loop is observed at the highest scan rate of 100 mV s^{-1}, with a maximum anodic current density value of approximately +0.23 mA cm^{-2} and a cathodic current density value of approximately −0.21 mA cm^{-2}. The preservation of the quasi-rectangular shape of the curve at this comparatively higher scan rate indicates efficient charge–discharge capability and negligible polarization.

The CV curves obtained for the silicon composite slurry deposited electrode over the graphite sheet substrate at different scan rates ranging from 25 mV s^{-1} to 100 mV s^{-1} within the potential range from −0.8 V to 1.4 V, as shown in Fig. 16F. At 25 mV s^{-1}, the curve displays a symmetric loop with smooth variations of current throughout the potential window. The charge storage is mainly controlled by the surface-regulated capacitive process, and the current variation becomes limited at this rate, suggesting slower ion transport near the electrode–electrolyte interface. At a scan rate of 50 mV s^{-1}, the magnitude of the current increases, resulting in a broader loop. Although the loop becomes broader with increased scan rate, the shape of the loop is preserved, indicating stable interfacial charge-transfer behaviour. When the scan rate is increased to 75 mV s^{-1}, the loop expands further, along with an increase in current density up to 1.45 mA cm^{-2}; this increase, along with the increase in scan rate, supports the electrical double layer formation rather than a bulk insertion process. At the highest scan rate of 100 mV s^{-1}, the curve shows the spread, with the current density ranging from −0.52 mA cm^{-2} to 0.68 mA cm^{-2}. The CV curve becomes more elongated due to the increased polarization effects, along with the accelerated ion shifting at the interface of the electrode.

The cyclic voltammetry (CV) curves of the silicon composite slurry-coated copper foil electrode measured at a scan rates of 5 mV s^{-1} and 10 mV s^{-1} show non-rectangular shapes with broad cathodic and anodic features, highlighting the charge-storage mechanism involving both faradaic reactions combined with capacitive behaviours (Fig. 16A). Lithium ions are inserted into the silicon framework to form Li_xSi phases during the cathodic scan, whereas during the anodic sweep the de-lithiation process occurs within +0.3 V to +0.5 V, which confirmed the reversibility of the electrochemical process. The broad nature of redox peaks reveals the composite structure of the material, along with its partial amorphous nature due to the formation of silicon oxide during chemical treatment. The increase in the current response with the increasing scan rate is clearly observed from the curves, but the complete retention of the shape of the curve suggests electrochemical stability and reversibility.

The CV plots of the silicon composite slurry deposited over the ITO substrate, as shown in Fig. 16B, display non-rectangular-shaped curves, indicating a combination of electric double layer capacitance behaviour along with the faradaic redox processes. The presence of broad cathodic and anodic peaks reflects the distribution of surface-driven electrochemical reactions across various active sites within the composite material. A noticeable rise in current is observed with the increase in the scan rate from 5 mV s^{-1} to 10 mV s^{-1} because of the limitations in the diffusion process, along with the increment in the effects due to polarization.

Fig. 16C shows the cyclic voltammetry curves of the silicon composite slurry deposited over a graphite sheet. At a scan rate

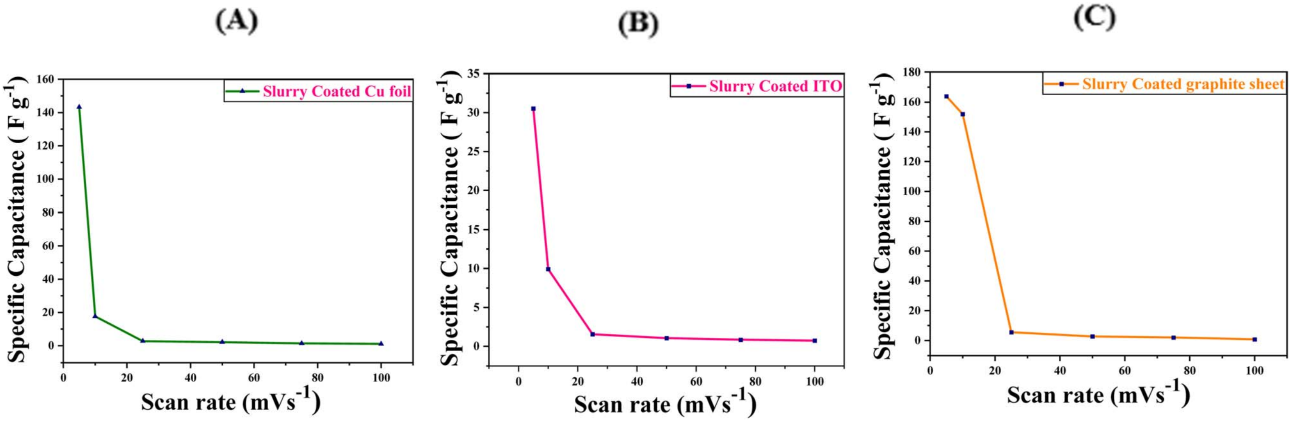

Fig. 17 Scan rate *vs.* specific capacitance plots of the slurry-coated (A) Cu foil electrode, (B) ITO substrate, and (C) graphite sheet electrode with scan rate ranging from 5 mVs^{-1} to 100 mVs^{-1}.

of 5 mV s^{-1}, the shape of the curve is non-rectangular, along with broad cathodic and anodic features that indicate the involvement of both surface capacitive effects as well as faradaic reactions. The lower scan rate allows enough time for the ions of the electrolyte to penetrate into the structure of the electrode, leading to better use of the active sites along with a more accurate electrochemical behaviour. When the scan rate is increased to 10 mV s^{-1}, an increment in the current density is observed, along with the expansion of the CV loop. At this higher scan rate, ion diffusion into the inner regions of the electrode becomes restricted, and the electrochemical process is increasingly governed by surface-controlled reactions. In addition, a minor shift in the oxidation and reduction peaks occurs because of the polarization effects and internal resistance within the electrode system.

The specific capacitance (C_p) values for coated Cu foil, ITO and graphite sheet were calculated from the CV plots at different scan rates. The maximum value of specific capacitance for the Cu foil electrode was 143.23 F g^{-1}, which was achieved at a scan rate of 5 mV s^{-1}. The maximum specific capacitances for ITO and graphite sheet were 30.53 F g^{-1} and 163.92 F g^{-1}, respectively, at a scan rate of 5 mV s^{-1} (Fig. 17).

4.5 Electrochemical impedance spectroscopy analysis

Fig. 18A shows the Nyquist plot of the electrode made over copper foil. The impedance curve shows a semicircle in the high-to medium-frequency regions followed by an inclined line in the low-frequency region, implying lithium-ion diffusion behaviour. In the high-frequency region, the intercept of the Nyquist plot on the Z'-axis corresponds to a solution resistance (R_s) of $\sim$20 Ω, which mainly occurs due to the resistance of the electrolyte and the internal interface. In addition to this, the occurrence of a distinct semicircle in the mid-frequency region indicates a charge-transfer resistance (R_{ct}) of $\sim$290 Ω, which arises because of the limited lithium-ion exchange and charge-transfer reactions between the active material and the electrolyte. At low frequencies beyond the semi-circular portion, the Nyquist plot shows a nearly vertical inclination from $\sim$37.62 Ω to $\sim$331.42 Ω, which shows the characteristics of Warburg impedance related to the movement of Li^+ ions in the bulk of the electrode. This region in the plot shows efficient ion transport through the porous silicon network along with the minor diffusion resistance, most likely due to the repeated volume change of silicon during lithiation and de-lithiation.[41,42]

Fig. 18B represents the Nyquist plot of the coated ITO substrate electrode. This impedance curve also consists of a semicircular loop in the high-to mid-frequency regions, followed by a sharply increasing tail in the low-frequency region. In the high-frequency region, the intercept of the Nyquist plot on the Z'-axis represents the solution resistance (R_s), which is around $\sim$114 Ω. This resistance occurs mainly from the collective effect of the electrolyte, the surface of the ITO substrate, and the electrode–electrolyte interface. Along with this, the presence of a relatively flattened semicircle in the mid-frequency region describes a charge-transfer resistance (R_{ct}) of $\sim$187.12 Ω, which is because the electrode–electrolyte interface is regulated by a combination of surface interactions. In the low-frequency region beyond the semicircular portion, the plot rises sharply upward by forming a Warburg-type inclination related to the ion diffusion through the porous structures. Therefore, the EIS plot shows moderate charge-transfer resistance, along with the diffusion-controlled charge dynamics within the silicon composite layer over the ITO substrate.

The EIS plot of the silicon composite slurry-coated graphite sheet describes a distinctly different set of characteristics compared to the other substrates. The Nyquist plot shows an almost linear plot extending from the high-to the low-frequency regions, with a very small solution resistance value (R_s) of $\sim$10 Ω. The very small size of the semicircle indicates that the charge-transfer resistance at the graphite sheet and electrolyte interface describes the high electrical conductivity of the graphite substrate, along with the continuous conductive pathway formed by the silicon composite slurry. At the low-frequency portion, the linear tail confirms that the ion migration process occurs through the porous electrode structure, and the electrolyte contributes to the overall impedance.

The equivalent circuits shown in Fig. 18D–F for the three fitted electrochemical impedance spectra are also shown with their respective fitted plots. The circuits consist of elements including R_1, which represents solution resistance, R_2, which represents surface resistance, R_3, which is the charge transfer resistance, and C_1 and C_2 are the double layer capacitance and pseudocapacitive contribution, respectively. Also, W_{01} stands for the finite Warburg element, whereas W_1 and W_2 are the semi-infinite Warburg elements. CPE stands for the constant phase element showing non-ideal capacitive behaviour.

Fig. 18G–I show the Bode plots for the slurry deposited over cu foil, ITO and graphite sheet, respectively, which provide an additional understanding of the frequency-dependent impedance characteristics of the electrodes. At lower frequencies, in the case of the Cu foil substrate, the impedance is relatively high, indicating slower charge-transport processes and significant interfacial resistance. With the increase in frequency, the impedance drops sharply and eventually approaches a low, frequency-independent region, which signifies improved charge accommodation at higher frequencies. The phase-angle curve displays a noticeable peak around the mid-frequency range.

The silicon composite slurry deposited over the ITO substrate electrode exhibits high impedance at low frequencies, showing reduced ion mobility and prominent interfacial polarization effects during slowly varying signals. As the frequency increases, the magnitude of the impedance decreases and transitions into a more stable region. The phase-angle plot shows a well-defined peak in the mid-frequency range, describing a distinct relaxation process associated with interfacial charge redistribution and surface-dominated kinetics. The position and shape of this peak reflect faster electrochemical characteristics than the observed peak in the plot of the Cu foil substrate.

In the case of the graphite sheet, in the low-frequency region, the magnitude of the impedance is very low. This type of curve suggests faster charge transport within the graphite network. The decrease in impedance with the increase in frequency is

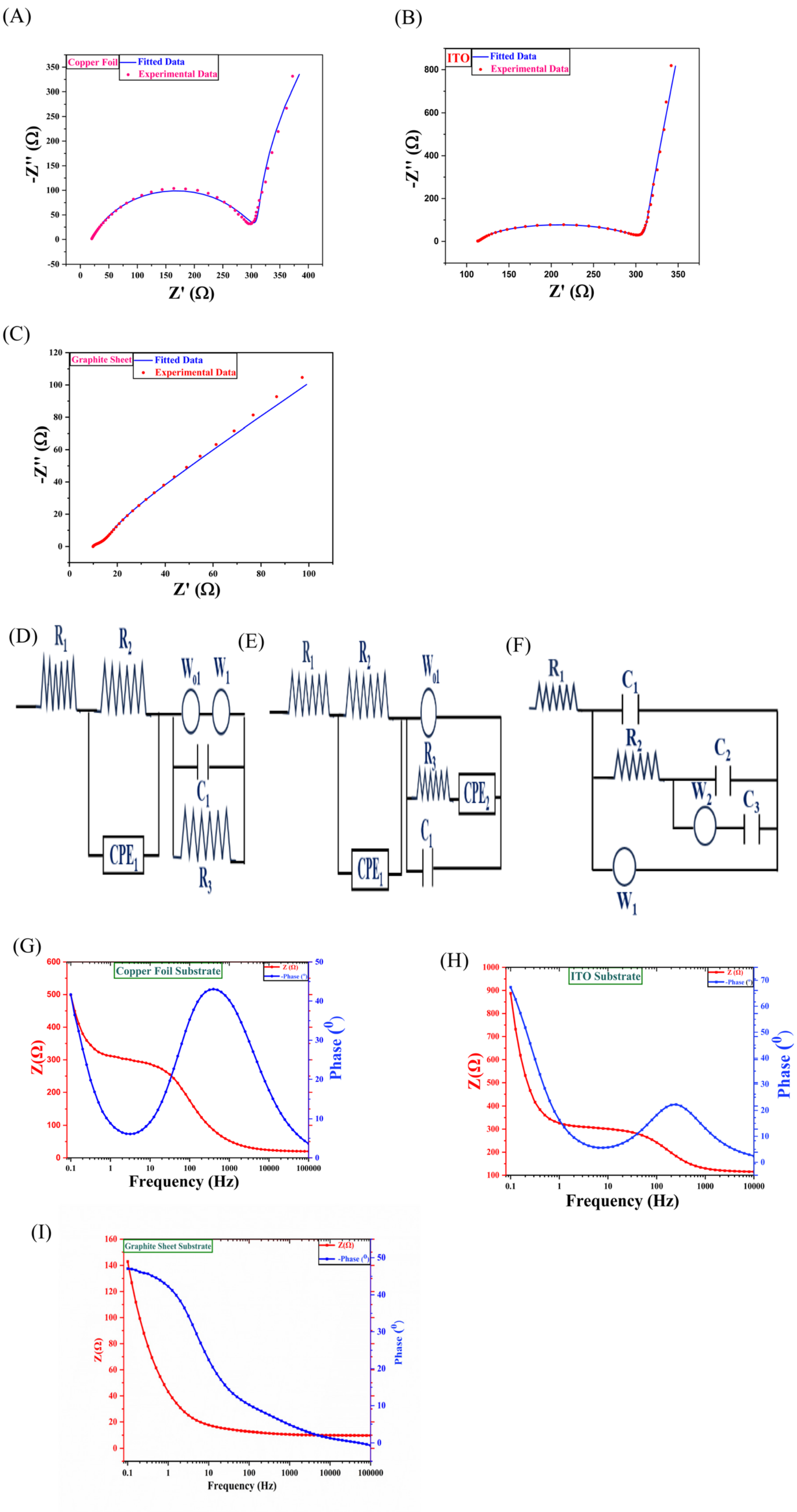

Fig. 18 Electrochemical impedance spectroscopy (EIS) analysis of slurry-coated electrodes: (A) Nyquist plot of the slurry-coated Cu foil electrode showing experimental data along with the fitted curve. (B) Nyquist plot of the slurry-coated ITO substrate with corresponding fitted data. (C) Nyquist plot of the slurry-coated graphite sheet electrode as well as the fitted plot. Equivalent circuit image used to fit the data of (D) Cu foil electrode, (E) ITO substrate electrode, and (F) graphite sheet electrode. Bode plots of slurry-coated electrodes showing impedance magnitude (*Z*) and phase angle (°) as a function of frequency for (G) slurry-coated Cu foil electrode, (H) slurry-coated ITO substrate, and (I) slurry-coated graphite sheet electrode. In each plot, the red curves represent the impedance magnitude (*Z*), while the blue curves correspond to the phase angle (°). The frequency ranges from 0.1 Hz to 10 KHz for Cu foil and ITO substrate electrode and 0.1 Hz to 100 KHz for the graphite sheet electrode, illustrating the charge-transfer behaviour, interfacial characteristics and frequency-dependent electrochemical response of the respective electrodes.

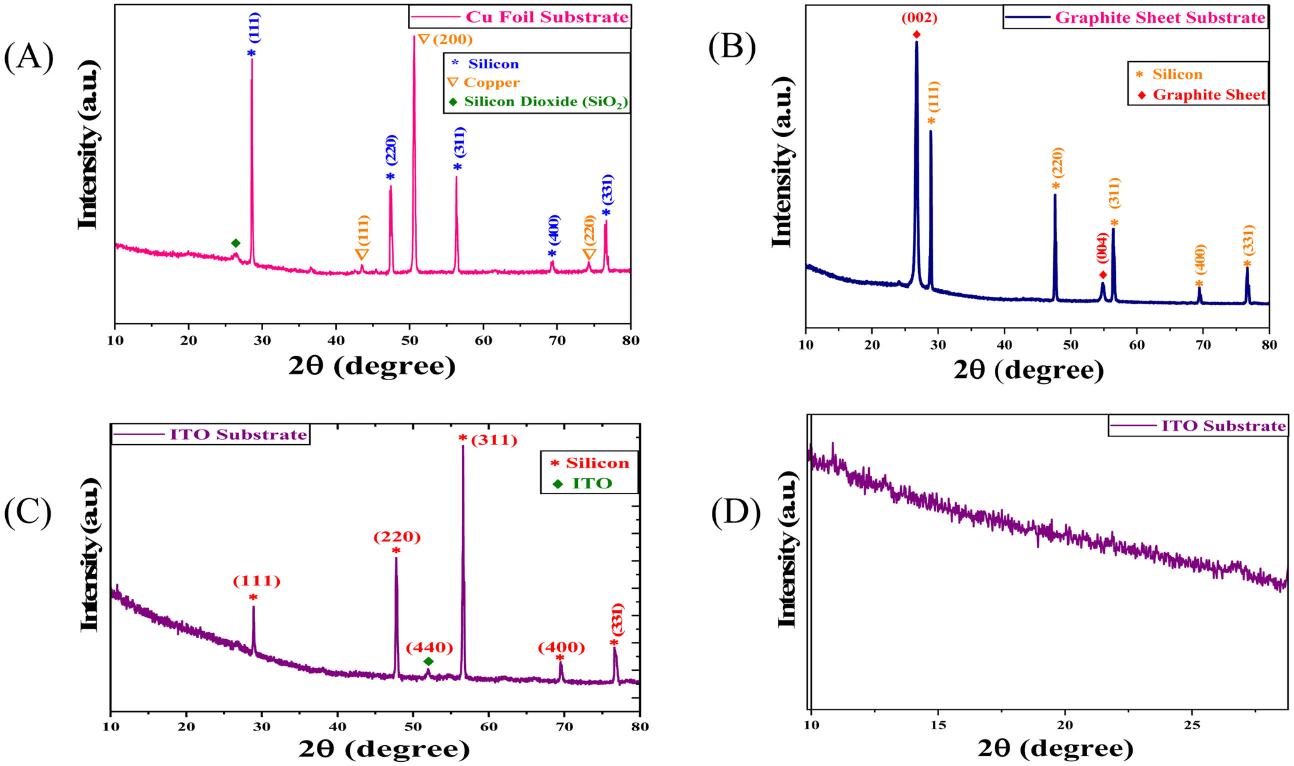

Fig. 19 X-ray diffraction (XRD) patterns of the recycled Si/SiO_2 composite electrodes deposited on different substrates after post-GCD (galvanostatic charge–discharge) cycling: (A) Cu foil substrate, (B) graphite sheet substrate, and (C) ITO substrate. (D) Plot showing the broad diffused background due to the presence of amorphous phases.

more uniform than that of the other substrates. The phase-angle peak appears at much lower impedance values and the Bode plot clearly establishes the graphite sheet substrate as the most conductive among the three.

The obtained χ^2 values from the EIS fitted data are 1.794 for the graphite sheet, 2.205 for Cu foil and 8.141 for ITO-based electrodes. The relatively low χ^2 values in the case of graphite sheet and ITO substrate-based electrodes indicate a close agreement between the experimental data and fitted data. A slightly higher χ^2 value in the case of the ITO-based electrodes is due to the possible surface oxidation and non-ideal electrode–electrolyte interactions. In addition, a comparison table consisting of R_s, R_{ct} and Warburg parameters for all three types of electrodes in this Table 2.

4.6 Post-cycling X-ray diffraction spectroscopy analysis

The post-cycling XRD measurements were performed after repeated electrochemical cycling to investigate the structural changes in the electrode material. After 500 GCD cycles, the XRD patterns show some significant changes in the structural characteristics of all three types of electrodes. The diffraction patterns, shown in Fig. 19A–C, are composed of slightly broadened and less intense crystalline silicon peaks compared to those of the XRD peaks of the pre-cycling electrodes, suggesting partial loss of crystallinity, along with the occurrence of structural disorder due to the repeated lithiation and de-lithiation cycles. Meanwhile, in the case of the Cu foil electrode, the sharp and intense peaks of the copper substrate confirm its structural stability during cycling. Similarly, in the case of the graphite sheet electrode, the most prominent peak at ~26.8° and a minor peak at 54.9° correspond to the (002) and (004) planes of the graphite substrate. The XRD plot of the ITO-based electrode highlights the presence of a peak due to the ITO substrate at ~52° that corresponds to its (440) plane. Furthermore, the presence of a broad hump at ~26.5° only in the case of Cu foil electrode, showcases the characteristics of amorphous SiO_2, suggesting that the SiO_2 network remains structurally stable and plays a critical role in accommodating volume changes during cycling. The absence of prominent peaks related to lithium–silicon alloy phases in all three plots suggests that such phases are either non-crystalline or undergo structural loss after de-lithiation. Again, the presence of a broad diffused background, as displayed in Fig. 19C, shows the presence of amorphous phases, which might be attributed to the Li_xSi and surface solid–electrolyte interface layers formed during continuous lithiation and de-lithiation processes.

Table 2 A comparison of R_s, R_{ct} and Warburg parameters for various electrodes

Substrate type	R_S (Ω)	R_{ct} (Ω)	Warburg parameter	χ^2
Graphite sheet	9.88	16.03	$A_{w1} = 80.438$ $A_{w2} = 105.08$	1.794
Copper foil	19.77	290.55	$A_{w1} = 2.856$ $W_{or1} = 28.805$	2.205
ITO	114.11	187.12	$W_{or1} = 236.64$ $W_{or2} = 0.309$	8.141

5 Conclusion

In summary, we have illustrated a simple and less toxic approach to recycling silicon solar cells to produce Si/SiO_2 composite powder. The recycled composite powder was found to have 99.52% purity with respect to silicon. This powder, with the addition of CNTs and PVDF–NMP binder, was then deposited over three different substrates, which exhibited fine electrochemical performance with an appreciable reversible capacity. The electrochemical analysis also revealed distinct charge-storage mechanisms for the different current collectors. The electrodes prepared over copper foil and ITO showcased the characteristics of diffusion-controlled battery-type behaviour, whereas the graphite substrate-based electrode indicated capacitive charge-storage properties. Cyclic voltammetry and electrical impedance spectroscopy measurements show good interfacial characteristics, while galvanometric charge–discharge exhibited stable performance over 500 cycles. The specific capacitance values for deposited Cu foil, ITO and graphite sheet electrodes were calculated to be 143.23 Fg^{-1}, 30.53 Fg^{-1} and 163.92 Fg^{-1}, respectively. The close agreement between the fitted plot and experimental plots for electrodes prepared over different substrates shows the reliability of the experimental results. Therefore, we found that the electrodes made over copper foil and ITO are applicable for silicon-based electrodes in Li-ion electrochemical systems, whereas the graphite substrate electrode can be a promising electrode in sustainability-driven energy-storage applications. Further work will focus on the use of water-soluble binders, which allow environmentally friendly electrode fabrication, along with enhanced performance of the electrode by increasing cycling stability.

Author contributions

Soumya Ranjan Nayak: experimental investigation, methodology, validation, formal analysis, data curation, writing – original draft; Manisha Balkhandia: data curation and formal analysis; Imran Chhimpa: data curation and formal analysis; Sushil Kumar: conceptualization, visualization, validation, methodology, resources, supervision, data curation, writing – review and editing.

Conflicts of interest

There are no conflicts to declare.

Data availability

Data will be made available on request.

Supplementary information (SI) is available. See DOI: https://doi.org/10.1039/d6su00083e.

Acknowledgements

The authors are very thankful to the Director, CSIR, National Physical Laboratory, New Delhi, for his kind support. One of the authors, Soumya Ranjan Nayak, would like to acknowledge the University Grants Commission (UGC), Govt. of India, for providing a Senior Research Fellowship (SRF). The authors are thankful to Mr Jai S. Tawale (CSIR-NPL) for FESEM characterization, Mr Naval Kishore Upadhyaya for XRD characterization, Mr Umesh Garnaik for Raman spectroscopy characterizations, and Miss Ishika Aggarwal for GCD characterizations.

References

1 W. Akram, S. Salim, A. A. Al-Ghamdi, A. M. Kannan, A. Ahmed and H. Al-Salih, A review of life cycle assessment and sustainability analysis of photovoltaic recycling and disposal, *RSC Sustain.*, 2025, **3**, 21–36.

2 G. Wei, Y. Zhou, Z. Hou, Y. Li, Q. Liu, J. Chen and D. He, Review of c-Si PV module recycling and industrial feasibility, *Polar Res.*, 2025, **1**, 9–29.

3 R. Deng, P. R. Dias, M. Monteiro Lunardi and J. Ji, A sustainable chemical process to recycle end-of-life silicon solar cells, *Green Chem.*, 2021, **23**, 10157–10167.

4 S. Kim, J. Kim, S. Cho, K. Seo, B.-Uk Park, H.-S. Lee and J. Park, Development of eco-friendly pretreatment processes for high-purity silicon recovery from end-of-life photovoltaic modules, *RSC Adv.*, 2024, **14**, 31451–31460.

5 J. Park and N. Park, Wet etching processes for recycling crystalline silicon solar cells from end-of-life photovoltaic modules, *RSC Adv.*, 2014, **4**, 34823–34829.

6 H. Yang, Y. Li, W. Chen, C. Zhang, L. Huang and X. Luo, Scalable synthesis of a Si/C composite derived from photovoltaic silicon kerf waste toward anodes for high-performance lithium-ion batteries, *Energy Fuels*, 2024, **38**(6), 5121–5130.

7 J. Qiu, C. Zhu, B. Ge, Y. Wang, Z. Zhang, J. Han, P. Shi and Y. Liu, Manufacturing lithium-ion anodes from silicon recovered from end-of-life solar panels, *Appl. Surf. Sci.*, 2025, **682**, 161605.

8 Global Market Outlook for Solar Power 2025-2029, 2025, https://www.solarpowereurope.org/insights/outlooks/global-market-outlook-for-solar-power-2025-2029/detail.

9 F. C. S. M. Padoan, P. Altimari and F. Pagnanelli, Recycling of end-of-life photovoltaic panels: a chemical perspective on process development, *Sol. Energy*, 2019, **177**, 746–761.

10 P. Achievements, *Installed Solar Power Energy Capacity as of 31st December*, 2025.

11 S. Weckend, A. Wade and G. Heath, *End-of-life Management: Solar Photovoltaic Panels*, International Renewable Energy Agency (IRENA) and International Energy Agency Photovoltaic Power Systems Programme (IEA PVPS), 2016.

12 https://www.irena.org, Report 26 March 2025.

13 M. Mottaghi, A. Kulkarni and J. M. Pearce, Recycling silicon photovoltaic cells into silicon anodes for Li-ion batteries using 3D printing, *RSC Sustain.*, 2025, **3**, 1859–1869.

14 X.-B. Zhong, Y.-X. Song, Y.-H. Zhang, Y.-G. Zhang, X.-G. You, Pu-G. Ji, K. M. Shodievich, U. Khalilov, G.-K. Wang, X. Zhang, X.-L. Yao, F. Li, J.-F. Liang and H. Wang, Regeneration of photovoltaic industry silicon waste toward high-performance lithium-ion battery anode, *Rare Met.*, 2024, **43**(10), 4948–4960.

15 Z. Dong, J. Li, P. Ge and Y. Yang, Upcycling of long-term Si/C composites by introducing interfacial chemical bonds from spent solar photovoltaic and lithium-ion batteries, *Green Chem.*, 2025, **27**, 11914.

16 Z. Zhang, N. Yang, F. Xi, X. Chen, S. Li, W. Ma, Y. Lei and R. Deng, Purification of silicon from waste photovoltaic cells and its value-added application in lithium-ion batteries, *New J. Chem.*, 2022, **46**, 11788.

17 H. Ji, J. Li, S. Li, Y. Cui, Z. Liu, M. Huang, C. Xu, G. Li, Y. Zhao and H. Li, High-Value Utilization of Silicon Cutting Waste and Excrementum Bombycis to Synthesize Silicon–Carbon Composites as Anode Materials for Li-Ion Batteries, *Nanomaterials*, 2022, **12**(16), 2875.

18 O. Wang, Z. Chen and X. Ma, Advancing sustainable end-of-life strategies for photovoltaic modules with silicon reclamation for lithium-ion battery anodes, *Green Chem.*, 2024, **26**, 3688–3697.

19 H. Ji, Z. Liu, X. Li, J. Li, Z. Yan and K. Tang, Recycling Silicon Waste from Photovoltaic Industry to Prepare Yolk-Shell Si@void@C Anode Materials for Lithium ion batteries, *Processes*, 2023, **11**(6), 1764.

20 M. M. Rahman, A. Nelson, S. Mateti, Y. Chen and Qi Han, Photovoltaic Recycled Nano Silicon-Silica Based Anode to Enhance Lithium-Ion Battery Performance, *SSRN Electron. J.*, 2024, 1–27.

21 C. Zhang, J. Li, Y. Feng, G. Du, Y. Liu, Y. Wang, Y. Wang, Z. Wu, P. Yang, A. Nanjundan, K. Yang, X. Zhu and L. Zhang, Recycling silicon cutting waste from photovoltaic industry into high-performance anodes for lithium-ion batteries, *ACS Sustain. Chem. Eng.*, 2024, **12**(37), 14099–14108.

22 L. Shen, K. Sun, F. Xi, Z. Jiang, S. Li, Y. Wang, Z. Tong, J. Lu, W. Ma, M. A. Green and X. Hao, Conversion of photovoltaic waste silicon into amorphous Si nanowires for lithium-ion battery anodes, *Energy Environ. Sci.*, 2025, **18**, 4348–4361.

23 M. R. Kaiser, Z. Han, J. Liang, S.-X. Dou and J. Wang, Lithium sulfide-based cathode for lithium-ion/sulphur battery: recent progress and challenges, *Energy Storage Mater.*, 2019, **19**, 1–15.

24 F. Dou, Y. Weng, Q. Wang, G. Chen, H. Liu, L. Shi and D. Zhang, In situ imaging analysis of the inhibition effect of functional coating on the volume expansion of silicon anodes, *Chem. Eng. J.*, 2021, **417**, 128122.

25 B. Chen, L. Chen, L. Zu, Y. Feng, Q. Su, C. Zhang and J. Yang, Zero-Strain High-Capacity Silicon/Carbon Anode Enabled by a MOF-Derived Space-Confined Single-Atom Catalytic Strategy for Lithium-Ion Batteries, *Adv. Mater.*, 2022, **34**(21), 2200894.

26 Y. Zhang, W. Yang, X. Liu, G. Ma, G. Hu, Z. Liu, R. Yu, D. Zhuang, J. Xu, D. Zhao, L. Mai and L. Zhou, Necklace-Structured Silicon Suboxide-Based Anode Materials with Multiple Carbon Networks for Stable Lithium Storage, *Adv. Funct. Mater.*, 2024, **34**, 2315680.

27 X. Fan, T. Cai, S. Wang, Z. Yang and W. Zhang, Carbon Nanotube-Reinforced Dual Carbon Stress-Buffering for Highly Stable Silicon Anode Material in Lithium-Ion Battery, *Small*, 2023, **19**(30), 2300431.

28 H. Kang, J. Ko, S. Song and Y. Yoon, Recent Progress in Utilizing Carbon Nanotubes and Graphene to Relieve Volume Expansion and Increase Electrical Conductivity of Si-Based Composite Anodes for Lithium-Ion Batteries, *Carbon*, 2024, **219**, 118800.

29 C. Zhu, J. Qiu, Y. Wang, S. Gong, Y. Min and Y. Liu Penghui Shi, Recycling Co and Li from spent lithium-ion batteries using the silicon of spent photovoltaic panels, *New J. Chem.*, 2025, **49**, 8675–8685.

30 O. Wang and X. Ma, Innovating the recycling of silicon-based solar panels with an eco-friendly alkaline leaching process, *Resour. Conserv. Recycl.*, 2024, **211**, 107887.

31 D. Sah and S. Kumar, Experimental, cost and waste analysis of recycling process for crystalline silicon solar module, *Sol. Energy*, 2024, **273**, 112534.

32 D. Sah, Chitra and S. Kumar, Recovery and analysis of valuable materials from a discarded crystalline silicon solar module, *Sol. Energy Mater. Sol. Cells*, 2022, **246**, 111908.

33 W.-J. Lee and Y.-H. Chang, Growth without Post-annealing of Monoclinic VO_2 Thin Film by Atomic Layer Deposition Using VCl_4 as Precursor, *Coatings*, 2018, **8**, 431.

34 S. Kodan, A. Kumar, A. Sanger, A. Arora, V. K. Malik and R. Chandra, Vertically aligned MoSe2-WS2 nano worms heterojunction towards room temperature NO2 gas sensors, *Sens. Actuators, B*, 2024, **407**, 135481.

35 B. Jabeen and U. Rafique, Synthesis and Application of Metal Doped Silica Particles for Adsorptive Desulphurization of Fuels, *Environ. Eng. Res.*, 2014, **19**(3), 205–214.

36 D. Sah, Chitra, N. Upadhyay, S. Muthiah and S. Kumar, Growth and analysis of polycrystalline silicon ingots using recycled silicon from waste solar module, *Sol. Energy Mater. Sol. Cells*, 2023, **261**, 112524.

37 Z. Yang, X. Gong, B. Wang, D. Yang, T. Fu and Y. Liu, Efficient in situ generation of H2O2 by novel magnesium–carbon nanotube composites, *RSC Adv.*, 2018, **8**, 35179–35186.

38 S. Kim, S. Ha, J. Lee, Y. Jeon and J. Hong, Preparation of Silicon Oxide-Carbon Composite with Tailored Electrochemical Properties for Anode in Lithium-Ion Batteries, *Journal of Carbon Research*, 2023, **9**, 114.

39 H. Kim, S. Yeo, M. Kim and G. Lee, Advancing silicon-based Li-ion batteries: enhanced stability and performance through carbon-coated Si and rGO linkage, *J. Mater. Sci.*, 2023, **58**, 13621–13634.

40 H. Wu, L. Zheng, J. Zhan, N. Du, W. Liu, J. Ma, L. Su and L. Wang, Recycling silicon-based industrial waste as sustainable sources of Si/SiO_2 composites for high-performance Li-ion battery anodes, *J. Power Sources*, 2020, **449**, 227513.

41 J. Sun, J. Jiang, Z. Xu, L. Su, X. Zou, C. Gao, Y. Cui, Z. Zhou, X. Wang, H. Pan and L. Cao, Design and development of a high-performance epoxidized polyvinyl alcohol/chitosan dual cross-linked composite binder for the effective suppression of Si anode volume expansion, *J. Power Sources*, 2025, **639**, 236670.

42 C. Chen, S. Lee, M. Cho, J. Kim and Y. Lee, Cross-Linked Chitosan as an Efficient Binder for Si Anode of Li-ion Batteries, *ACS Appl. Mater. Interfaces*, 2016, **8**(4), 2658–2665.